Synthesis, Structure, and Zero-Field SMM Behavior of Homometallic Dy2, Dy4, and Dy6 Complexes

Pawan Kumar, Abinash Swain, Joydev Acharya, Yanling Li, Vierandra Kumar, Gopalan Rajaraman, Enrique Colacio, Vadapalli Chandrasekhar

Synthesis, Structure and Zero-Field SMM Behavior of Homometallic Dy2, Dy4 and Dy6 Complexes

Pawan Kumar,[a] *Abinash Swain,*[b] *Joydev Acharya,*[a] *Y. Li,*[c] *Vierandra Kumar,*[a] *Gopalan Rajaraman,**[b] *Enrique Colacio**[d] *and Vadapalli Chandrasekhar**[a,e]

[a]Department of Chemistry, Indian Institute of Technology Kanpur, Kanpur-208016, India

[b]Department of Chemistry, Indian Institute of Technology Bombay, Powai, Mumbai 400076, India.

[c]Sorbonne Universit Institut Parisien de Chimie Molculaire, CNRS UMR 8232 4 place Jussieu 75252 Paris cedex 5 (France)

[d] Department of Inorganic Chemistry, University of Granada, 18071-Granada, Spain.

[e]Tata Institute of Fundamental Research Hyderabad, Gopanpally, Hyderabad-500 107, India

Abstract

The synthesis, structure and magnetic properties of three Dy^{III} complexes of different nuclerity, $[Dy_2(H_2L)_2(NO_3)]$ $[NO_3]\cdot$ $2H_2O\cdot CH_3OH$ (**1**), $[Dy_4(LH)_2(piv)_4(OH)_2]$ (**2**) and **[**$Dy_6(LH_2)_3(\mu_3$–OH)$(\mu_3$–$CO_3)_3(CH_3OH)_4(H_2O)_8]$ $5Cl\cdot 3H_2O$ (**3**) [(LH_4) = 6-((bis(2-hydroxyethyl)amino)-*N*'-(2-hydroxybenzylidene)picolinohydrazide) are described. This variety of complexes with the same ligand could be obtained by playing with the metal to ligand molar ratio, the type of Dy^{III} salt, the kind of base and the presence/absence of coligand. **1** is a dinuclear complex, while **2** is a tetranuclear assembly with a butterfly shaped topology. **3** is a homometallic hexanuclear complex that exhibits a propeller-shaped topology. Interestingly, in this complex **3**, three atmospheric carbon dioxide molecules are trapped in the form of carbonate ions which assist in holding the hexanuclear complex together. All the complexes reveal a slow relaxation of

magnetization even in zero applied field. Complex **1** is a zero-field SMM with an effective energy barrier (U_{eff}) of magnetization reversal equal to 87(1) K and relaxation time of $\tau_0 = 6.4(3) \times 10^{-9}$ s. Under an applied magnetic field of 0.1 T these parameters change to $U_{eff} = 101(3)$ K, $\tau_0 = 2.5(1) \times 10^{-9}$ s.Complex **2** shows zero field SMM behavior with $U_{eff} = 31(2)$ K, $\tau_0 = 4.2(1) \times 10^{-7}$ s while **3**, also a zero-field SMM, shows a double relaxation of magnetization [$U_{eff1} = 62(3)$ K, $\tau_{01} = 4.6(3) \cdot 10^{-8}$ s, and $U_{eff1} = 2(1)$ K, $\tau_{02} = 4(6) \cdot 10^{-5}$ s]. Ab initio calculations indicated that in these complexes the Kramers ground doublet is characterized by an axial g-tensor with prevalence of the $M_J = \pm 15/2$ component, as well as that, due to the weak magnetic coupling between the metal centres, the magnetic relaxation, ~~barrier~~ wich is dominated by the single Dy^{III} centres rather than the exchange-coupled state, takes place via Raman/Orbach or TA-QTM. Moreover, theoretical calculations support a toroidal magnetic state for complex **2**.

Keywords: lanthanide complexes**,** magnetic anisotropy**,** aryolohydrazone Schiff base, zero field, single molecule magnets, magnetic measurements, slow relaxation of magnetization

Introduction

There is considerable recent interest in the utility of appropriate lanthanide metal complexes as single molecule magnets (SMMs) and single-ion magnets (SIMs). This field got its breakthrough by the seminal discovery of Ishikawa and co-workers that the terbium phthalocyanine sandwich complex $[Bu_4N][TbPc_2]$ is a single molecule magnet with slow relaxation of magnetization.[1] This discovery prompted researchers to examine the favorable properties of lanathanide ions including a large unquenched spin-orbit coupling which can result in substantial single-ion

anisotropy.[2] In addition, many lanthanide ions have a reasonable ground state spin owing to the presence of large number of unpaired electrons. Finally, ions such as Dy^{III} are Kramers ions with a bistable ground state. Because of this a large number of Dy^{III} complexes have been examined and found to be single-molecule magnets.[3] This area got a further boost by the discovery that the organometallic sandwich complexes, $[Dy(Cp^{ttt})_2][B(C_6F_5)_4]$, where Cp^{ttt}= ($C_5H_2{}^tBu_3$-1,2,4), and $[(Cp^{iPr5})Dy(Cp^*)]^+$ (Cp^{iPr5}, penta-iso-propylcyclopentadienyl; Cp*, pentamethylcyclopentadienyl) show the highest blocking temperatures, temperatures below which the magnetization of the complexes is retained or blocked indefinitely.[4] These and other such organometallic complexes, while possessing extremely interesting magnetic properties are however, extremely air- and moisture sensitive rendering their handling difficult. Air-stable complexes are therefore of interest and there have been some examples of mononuclear complexes with good properties.[5] We have also been involved in such endeavors and have been to assemble mononuclear complexes in pentagonal bipyramidal and other geometries.[6]

In addition to mononuclear complexes, complexes with larger nuclearity have also been of interest because of a variety of reasons. Dinuclear complexes offer an opportunity to study the magnetic interactions between the two lanthanide centers.[7] Larger nuclearity complexes, particularly those containing Gd^{III} have attracted interest because of the possibility of harnessing magnetocaloric effect.[8] Lastly there has also been of interest to understand the design of ligands which allows a modulation of the nuclearity of the complexes as well as the coordination number and structural topology.Towards this end, we have been interested to probe whether a given ligand, under small variation of reaction conditions including using co-ligands or by stoichiometry or by varying the amount of base, can be used to assemble the complexes with varying nuclearity.

In this regard, the aroylhydrazone-based Schiff base ligands are quite remarkable. These ligands have suitable flexible coordination pockets involving C-C/C-N/N-N bond rotations which allows a flexible coordination response. In addition, these ligands also have the flexibility of binding to the metal ions either in their keto form or on the enol form depending upon the reaction conditions.[9]

Because of these interesting features we have been working with this family of ligands for some time with considerable success.[9] Recently we have used one member of this family to assemble a dinuclear Dy^{III} complex where the two Dy^{III} are non-equivalent.[9e]

Motivated by the above result we were interested in the possibility of using this ligand, LH_4, [(LH_4) = 6-((bis(2-hydroxyethyl)amino)-*N*'-(2-hydroxybenzylidene)picolinohydrazide) and examine if the *same* ligand under different reaction conditions can allow the assembly of complexes with varying nuclearity. This is a concept that we have explored earlier[9c] and were interested to see its implementation with LH_4. Accordingly, herein, we report the synthesis, structural characterization and magnetic studies of, $[Dy_2(LH_2)_2(NO_3)]$ NO_3 $2H_2O$ CH_3OH(**1**), $[Dy_4(LH)_2(piv)_4(OH)_2]$(**2**) and **[**$Dy_6(LH_2)_3(\mu_3–OH)(\mu_3–CO_3)_3(CH_3OH)_4(H_2O)_8]$ $5Cl\cdot3H_2O$(**3**). Detailed magnetic studies reveal that **1-3** are zero-field SMMs.

Experimental Section

Solvents and other general reagents used in this work were purified according to standard procedures.[10] Pyridine–2,6-dicarboxylic acid, sodium borohydride, pivalic acid, tetrabutyl ammoniumhydroxide solution (40 wt % in water), $DyCl_3\cdot6H_2O$ and $Dy(NO_3)_3\cdot5H_2O$ were obtained from Sigma Aldrich Chemical Co. and were used as received. Hydrazine hydrate (80%), diethanolamine, PBr_3 and sodium sulphate (anhydrous) were obtained from SD. Fine Chemicals, Mumbai, India.

Instrumentation

Melting points were measured using a JSGW melting point apparatus and are uncorrected. IR spectra were recorded as KBr pellets on a Bruker Vector 22 FT IR spectrophotometer operating between 400–4000 cm^{-1}. Elemental analyses of the compounds were obtained by using Thermoquest CE instruments CHNS-O, E.A./110 model. ESI-MS spectra were recorded on a MICROMASS QUATTRO II triple quadrupole mass spectrometer. ^{1}H NMR spectra were recorded in $CDCl_3$ and DMSO-d^6 solutions on a JEOL JNM LAMBDA 400 model spectrometer operating at 500.0 MHz, Chemical shifts are reported in parts per million (ppm) and are referenced with respect to internal tetramethylsilane (^{1}H).

X-ray Crystallography

Single crystal data for **2** was collected on a Bruker *SMART* CCD diffractometer (MoK_α radiation, λ = 0.71073 Å) at 100 K. The program *SMART* [11a] was used for collecting frames of data, indexing reflections, and determining lattice parameters, *SAINT* [11a]for integration of the intensity of reflections and scaling, *SADABS* [11b] for absorption correction, and *SHELXTL* [11c]for space group and structure determination and least-squares refinements on F^2. X-ray diffraction data for complexes **1** and **3** were collected at 120 K by using a Rigaku diffractometer with graphite-monochromated molybdenum Kα radiation, λ = 0.71073 Å. Data integration and -reduction were processed with CrysAlisPro software.[11d].An empirical absorption correction was applied to the collected reflections with SCALE3 ABSPACK integrated with CrysAlisPro.The crystal structures were solved and refined by full-matrix least-squares methods against F^2 by using the program *SHELXL-2014* [11e] using *Olex-2* [11f] software. All the non-hydrogen atoms were refined with anisotropic displacement parameters. Hydrogen positions were fixed at calculated

positions and refined isotropically. The crystallographic figures were generated using *Diamond 3.1e* software.[11g] .

The crystal data, the cell parameters and ccdc information for all the complexes are given in Table 1.

Table 1. Crystal data and structure refinement parameters of **1-3**

	1	**2**	**3**
Formula	$C_{37}H_{48}Dy_2N_{10}O_{17}$	$C_{56}H_{76}Dy_4N_8O_{18}$	$C_{61}H_{99}N_{12}O_{37}Dy_6Cl_5$
g/mol	1229.85	1799.24	2744.77
Crystal system	Trigonal	Monoclinic	Monoclinic
Space group	R3*c*	$P2_1/n$	$P2_1/n$
***a*/Å**	27.990(4)	12.129(5)	20.341(3)
***b*/Å**	27.990(4)	16.468(5)	30.464(3)
***c*/Å**	28.498(4)	17.663(5)	20.356(3)
***α* (°)**	90	90	90
***β*(°)**	90	94.941(2)	112.736(2)
***γ*(°)**	120	90	90
***V*/Å^3**	19335(5)	3515(4)	11634.0(3)
Z	18	2	4
***ρ*$_c$/g cm^{-3}**	1.901	1.700	1.567
***μ*/mm^{-1}**	3.538	4.269	3.988
***F*(000)**	10944.0	1752.0	5304.0
Cryst size (mm^3)	0.11 × 0.09 × 0.06	0.14 × 0.11 × 0.07	0.24 × 0.21 × 0.17
***2θ* range (deg)**	5.042 to 56.598	8.154 to 50.052	8.18 to 52.044
Limiting indices	-37<=h<=37 -37<=k<=37 -37<=l<=38	-14<=h<=13 -19<=k<=19 -21<=l<=20	-25<=h<=25 -37<=k<=37 -25<=l<=25
Reflns collected	95658	26532	182119
Ind reflns	10681 [*R*(int)=0.0716]	6187 [*R*(int) =0.0724]	22821 [R(int) =0.0349]
Completeness to *θ* (%)	100	100	100
Refinement method	Full-matrix least-squares on F^2	Full-matrix least-squares on F^2	Full-matrix least-squares on F^2
Data/restraints/params	10681/13/615	6187/3/383	22821/87/1175
Goodness-of-	1.038	1.033	1.027

fit on F^2			
Final R indices [$I > 2\theta(I)$]	R_1 = 0.0321 wR_2 = 0.0680	R_1 = 0.0491 wR_2 = 0.1066	R_1 = 0.0204 wR_2 = 0.0486
***R* indices (all data)**	R_1 = 0.0443 wR_2 = 0.0723	R_1 = 0.0781 wR_2 = 0.1158	R_1 = 0.0220 wR_2 = 0.0492
CCDC no.			

Magnetic Properties

Static (dc) and dynamic (ac) magnetic susceptibility measurements were carried out using respectively a Quantum Design MPMS-XL-7 SQUID magnetometer and a PPMS-9 (ACMS option) ~~susceptometer~~ on a polycrystalline powder samples. The dc measurements were performed in the temperature range 2 - 300 K under a magnetic field of 0.5 T (20 - 300K) and 0.05 T (40 - 2K), whereas the ac measurements were carried out in the temperature range 2.5-15 K under an oscillating field of 10 Oe within the frequency range 50 – 279 Hz and of 3 Oe within the frequency range 354 – 10000 Hz, under static fields of 0 and 2000 Oe. The magnetic susceptibility values were corrected from the diamagnetism of the molecular constituents and of the sample holder. The sample (about 15 mg) wrapped into a piece of parafilm (about 25 mg) and packed in a polyethylene bag~~)~~ was pelletized in order to avoid the reorientation at low temperature and high field. It was introduced in the SQUID at 200 K under helium flow and frozen before purging under vacuum.

Computational Details

All the calculations were performed using the MOLCAS 8.2 suit program using CASSCF/RASSI-SO/SINGLE_ANISO/POLY_ANISO module on the X-ray obtained crystal structures without further modelling. A TZVP quality of basis set has been used for the metal ion, for the surrounding coordinating atom a DZV level and for the rest of the atoms SVP level of basis set has been used from ANO-RCC library. The relativistic effect has been taken into

consideration using the DKH Hamiltonian. Cholesky decomposition was utilized to save storage space generated by one integral. Active space of 9 electrons in 7 f orbitals taken for all calculations with 21 roots in the RASSI-SO step. First, single-ion anisotropy calculations have been performed on the individual Dy^{III} centres by replacing the other Dy^{III} ion with the Lu^{III} ions. The calculations were carried out on the entire complex without further modelling to attain the most reliable values. This gives the magnetic properties offered by the individual Dy^{III} centres. The aniso input taken from the single aniso calculations has been used in the POLY_ANISO module to gain insight into the overall magnetic properties of the complexes originating from the exchanged coupled states. The fitted exchange parameters were further verified by density functional calculations using Gaussian 16 package with the hybrid B3LYP/CSDZ/TZV methods by replacing the Dy^{III} with Gd^{III} and then rescaling it by multiplying with a factor of 5/7. For complex **2**, the dM/dH vs H plot seems to indicate the presence of an S-shape plot for the M vs H plot at very low field (see ESI). This behaviour points out the possibility of a mixed toroidal moment for the above complex. Hence, using the POLY_ANISO module, the toroidal behaviour for complex **2** has been investigated.

Synthesis

The Ligand LH_4 was prepared according to the procedure that we reported recently.[9e]

Synthesis of 1-3

$[Dy_2(LH_2)_2(NO_3)]\,[NO_3]\cdot 2H_2O\cdot CH_3OH$ (1)

$Dy(NO_3)_3\cdot 5H_2O$ (0.048g, 0.11 mmol) was added to a methanol solution (30 mL) of LH_4 (0.040g, 0.11 mmol) at room temperature affording a yellow colored solution. Then, triethylamine (0.046 mL, 0.33 mmol) was added and the reaction mixture was allowed to stir overnight at room temperature. The resulting solution was then filtered and the filtrate stripped off its solvent in

vacuo affording a solid yellow residue which was dissolved in methanol (5 mL) and kept for slow evaporation. Suitable X−ray quality crystals were formed within 3-4 days. Yield: 0.051 g, 76.1% (based on the Dy^{III} salt). Mp: >250 °C (d). IR (KBr) cm^{-1}: 3385 (br), 3205(br), 2971 (br), 1611 (s), 1557 (w), 1537 (s), 1477 (s), 1453 (w), 1429, 1384 (s), 1261 (w), 1199 (s), 1143 (s), 1068 (s), 1004 (w), 880 (s), 850 (s), 800 (w), 760 (s), 713 (w), 690 (s), 598 (s), 534 (s). Anal. Calcd. For C_{37} H_{48} Dy_2 N_{10} O_{17} (1232.1782): C, 36.14; H, 3.93; N, 11.39 Found: C, 36.05; H, 3.72; N, 11.19.

$[Dy_4(LH)_2(piv)_4(OH)_2]$ (2)

Solid $DyCl_3 \cdot 6H_2O$ (0.082g, 0.22 mmol) and LH_4 (0.040g, 0.11 mmol) were taken in methanol (30 mL) and then stirred for 5 minutes at room temperature. Then, tetrabutylammonium hydroxide (0.55 mmol) was added to this mixture in a dropwise manner. After 15 minutes pivalic acid (0.22 mmol) was added and the reaction mixture was stirred for 8 hours at room temperature. All the volatiles were removed from the reaction mixture in vacuo affording a semisolid yellow residue which was dissolved in a mixture of methanol (5 mL) and chloroform(2 ml) and kept for crystallization by slow evaporation. Suitable crystals were harvested in 2-3 days.

Yield: 0.047, 47.9%. IR (KBr) cm^{-1}: 3424 (br), 2959 (br), 2865 (br), 1612 (s), 1571 (w), 1556.33 (s), 1476 (s), 1425 (s), 1377(s), 1350 (s), 1227(s), 1195 (s), 1079 (s), 1014(w), 901 (s), 848 (s), 756 (s), 656 (w), 595 (s). Anal. Calcd. For C_{56} H_{76} Dy_4 N_{10} O_{17} (1804.2444): C, 37.13; H, 4.23; N, 7.73 Found: C, 36.91 ; H, 4.05; N, 7.751.

$[Dy_6(LH_2)_3(\mu_3–OH)(\mu_3–CO_3)_3(CH_3OH)_4(H_2O)_8]$ $5Cl \cdot 3H_2O$ (3)

$DyCl_3 \cdot 6H_2O$ (0.082g, 0.22 mmol) and LH_4 (0.040g, 0.11 mmol) were dissolved in methanol (30 mL) and then stirred vigorously for 10 minutes at room temperature. Then, triethylamine (0.33

mmol) was added slowly to the solution dropwise and the reaction mixture stirred for 7 hours. After this, the volatiles in the reaction mixture were removed in vacuo to afford a solid yellow residue which dissolved in a mixture of methanol (5 mL) and chloroform(5 ml) and kept for crystallization by slow evaporation. Suitable crystals were obtained in 2-3 days. Yield: 0.045 g, 45.4% (based on the Dy^{III} salt). Mp: >200 °C (d). IR (KBr) cm^{-1}: 3375 (br), 1616 (s), 1560 (w), 1536 (w), 1476 (s), 1441 (w), 1351 (s), 1262 (w), 1201 (w), 1151 (s), 1123 (w), 1081 (s), 1016 (s), 916 (w), 892 (w), 796 (w), 691 (w), 520 (s). Anal. Calcd. For C_{61} H_{99} Dy_6 N_{12} O_{37} Cl_5 (2750.0427): C, 26.69; H, 3.64; N, 6.12 Found: C 25.70; H, 4.15; N, 5.60.

Results and Discussion

Synthetic Aspects

As discussed above, the versatile coordination possibilities of the aroylhydrazone-based Schiff base ligands have been attracting our attention. We have utilized the ligand LH_4 in the current investigations. This ligand has broadly two coordination pockets: a pentadentate (2N, 3O) and a tridentate (2O, 1N) . In addition, the coordination can be influenced by the extent of de-protonation as well as the choice of keto vs enolate coordination. These features allowed us to assemble Dy_2, Dy_4 and Dy_6 complexes. In the case of Dy2 and Dy6 systems the ligand binds to the metal centre in its doubly deprotanated form $[LH_2]^{2-}$ while in Dy4 in its triply deprotonated form $[LH]^{3-}$. In the latter, one arm of diethanolamine is deprotonated. In all the complexes the ligand utilized the enolate oxygen to bridge two lanthanide centers (Scheme 1).

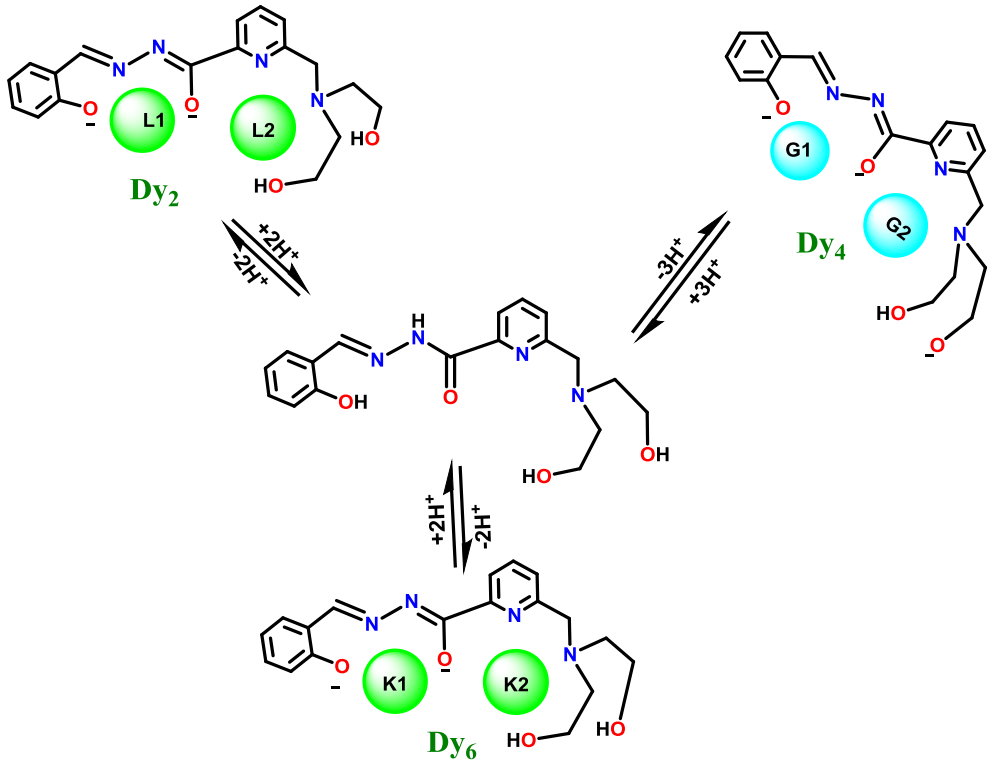

Scheme 1. Unsymmetrical coordination pockets, conformations based on base-assisted reversible keto-enol tautomerization and coordination modes of LH_4 as observed in complexes **1-3**.

The reaction of LH_4, $Dy(NO_3)_3{\cdot}5H_2O$ in the presence of Et_3N in a stoichiometric ratio of 1:1:2 in methanol at room temperature afforded a dinuclear complex $[Dy_2(LH_2)_2(\mu_2\text{-}\eta^1{:}\eta^1\text{-}NO_3)]{\cdot}NO_3{\cdot}2MeOH{\cdot}H_2O$ (**1**) (Scheme 2). On the other hand, by changing the metal to ligand ratio in the reaction of LH_4, $DyCl_3{\cdot}6H_2O$ in the presence of Et_3N in methanol with a stoichiometric ratio of 1:2:2 afforded hexanuclear complex, $[Dy_6(LH_2)_3(\mu_3\text{–}OH)(\mu_3\text{–}CO_3)_3(CH_3OH)_4(H_2O)_8]$ $5Cl{\cdot}3H_2O$(**3**) (Scheme 2). Changing the base from triethylamine to tetrabutylammonium hydroxide in the reaction of LH_4, $DyCl_3{\cdot}6H_2O$ along with pivalic acid as a co-ligand in a stoichiometric ratio of 1:2:2:5 afforded the tetranuclear complex $[Dy_4(LH)_2(\mu_3\text{-}OH)_2(Piv)_4]$(**2**) (Scheme 2).

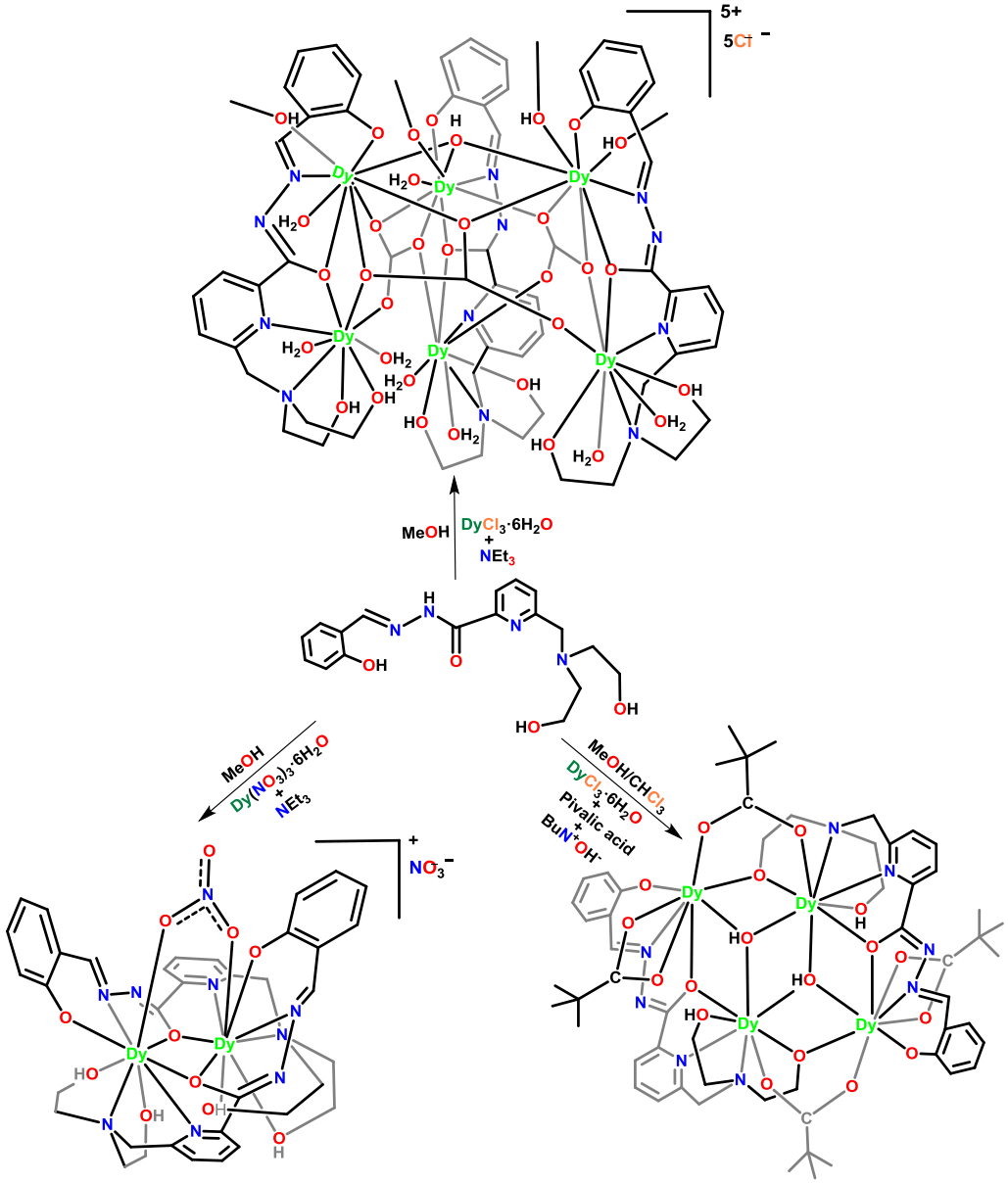

Scheme 2. Synthesis of **1**−**3**

It is interesting to note that in the presence of the stronger base tetrabutylamoniumhydroxide, in addition to deprotonation at the phenol and enol sites, one of the diethanolamine arms is also deprotonated. Along with a hydroxide ligand the deprotonated diethanolamine oxygens serve to connect the lanthanide centers that are present in a defect cubane structure (Scheme 2). The formation of the hexanuclear cluster is accomplished by the involvement of carbonate ligands

which is the result of activation of atmospheric CO_2. Formation of carbonate ligands in situ in such basic reaction conditions is not new. Uptake of atmospheric CO_2 as carbonate ligand has been reported for 3d, 3d-4f and 4f complexes.[12] We have ourselves observed this in the formation of tetranuclear lanthanide complex a few years ago (Figure 1).[12f]

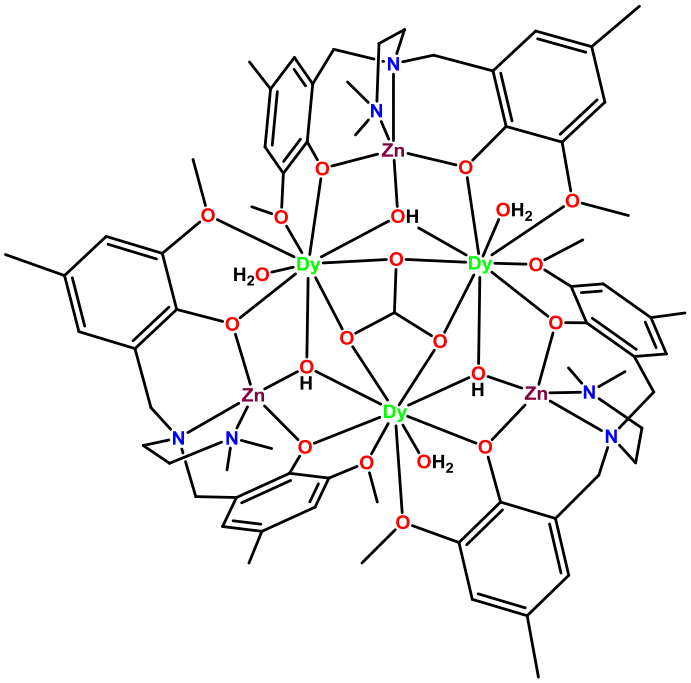

Figure 1. μ_3-CO_3 containing heterometallic hexanuclear complexes $[Zn_3Ln_3(\mu_6\text{-}CO_3)(\mu_3\text{-}OH)_3(L)_3(H_2O)_3]\cdot 3(ClO_4)\cdot NO_3$ [12f]

The various reported binding modes of carbonate ligand in the complexes given in Figure 2.

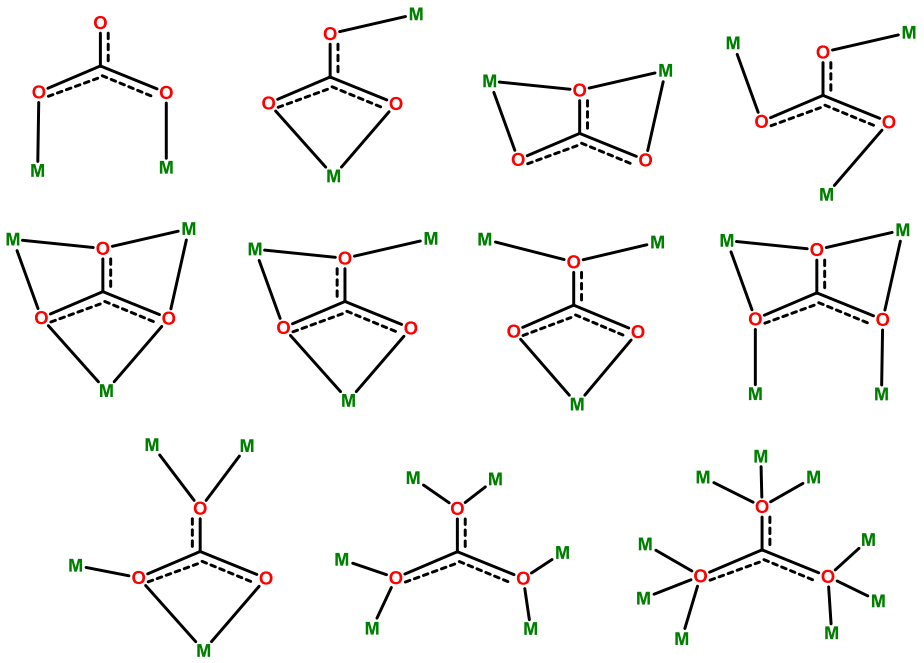

Figure 2. Some common binding modes of carbonate ligand in metal complexes[12]

In order to ascertain that the atmospheric CO_2 is indeed involved, we carried out the same reaction in completely inert conditions. We did not observe the formation of **3**. On the other hand when the reaction was performed in the presence of sodium carbonate, **3** was formed (Supporting Information). Identification of carbonate ligand in the complex **3** is done carefully by consideration of charge balance and SC-XRD crystal data. Absorption bands in the IR spectrum for **3** found at 1441 cm^{-1} and 839 cm^{-1} can be assigned for carbonate ligand. These absorptions bands are fully consistent with those observed other for carbonato complexes reported previously.[12f, 12h, 12k]

X-ray Crystallography

To elucidate the molecular structures of the complexes we carried out single crystal X-ray diffraction analysis. Complex **1** crystallized in the trigonal, *R*3c space group (Z = 18). The asymmetric unit consists of the full monocationic dinuclear motif $[Dy_2(LH_2)(\mu_2\text{–}NO_3)]^+$ along

with a nitrate counter ion. A perspective view of **1** is given in Figure 3 and the selected bond parameters are provided in caption of Figure 3.

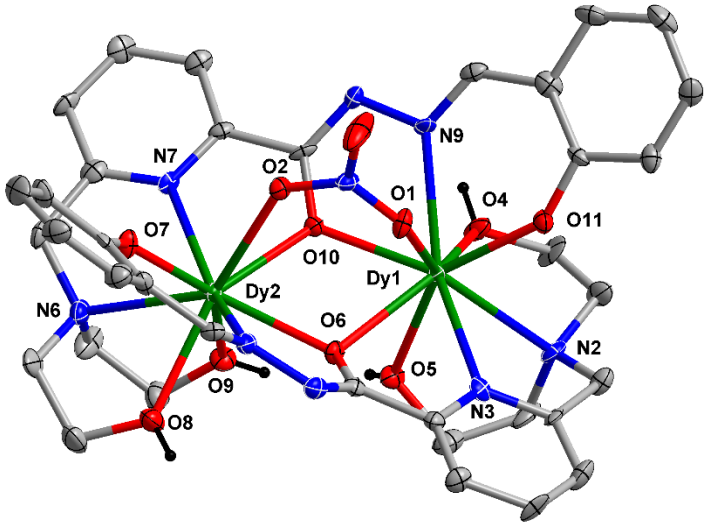

Figure 3. (a) Molecular structure of **1**. Thermal ellipsoids at 50% probability level are shown (selected hydrogen atoms and the solvent molecules have been omitted for clarity). Color codes: N = blue; O = red; C = grey; Dy= dark green and H = black). Selected bond lengths (Å) for **1**: for Dy1; Dy1–O1, Dy1–O4, Dy1–O5, Dy1–O6, Dy1–O10, Dy1–O11, Dy1–N2, Dy1–N3, Dy1–N9, are 2.469 (1), 2.420(9), 2.482(8), 2.500(5), 2.323(5), 2.183(6), 2.621(9), 2.508(5), 2.515(9), respectively, for Dy2; Dy2–O2, Dy2–O6, Dy2–O7, Dy2–O8, Dy2–O9, Dy2–O10, Dy2–N5, Dy2–N6, Dy2–N7 are 2.459(8), 2.323(5), 2.189(9), 2.450(7), 2.446(1), 2.506(5), 2.582(6), 2.528(1) respectively, and selected bond angles for **1**: Dy1–O10–Dy2, Dy1–O6–Dy2, are 110.65(2)°, 110.85(2)°, respectively.

The dinuclear assembly is built with the assistance of two doubly deprotonated LH_2^{2-} ligands. The two Dy^{III} centers are bound by the coordination pockets described above and are bridged by

the enolate oxygen atom (Figure 4). One of the nitrate anions bridges the two Dy^{III} centers, while the other remains as a counter anion. (Figure 4)

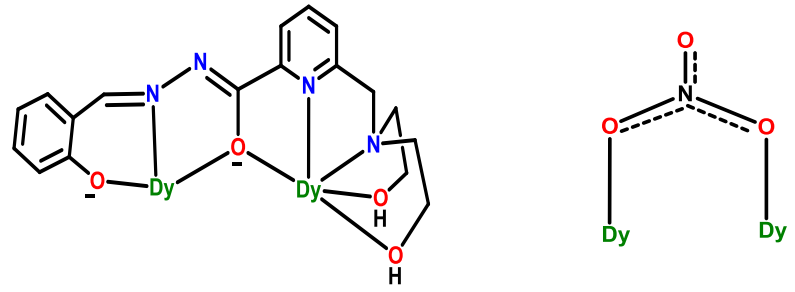

$\mu_2 - \eta^1: \eta^1: \eta^2: \eta^1: \eta^1: \eta^1: \eta^1$ $\mu_2 - \eta^1\ \eta^1$

Figure 4. Ligands coordination modes involved in the dinuclear assembly**.**

As can be seen from the above description, the formation of **1** involved the complete utilization of *all* the coordination sites of (LH_2^{2-}). The central Dy_2O_2 core is non-planar with a dihedral angle of 109.96(19)°(Figure 5**)**. The other metric parameters are given in the caption of the Figure 3.

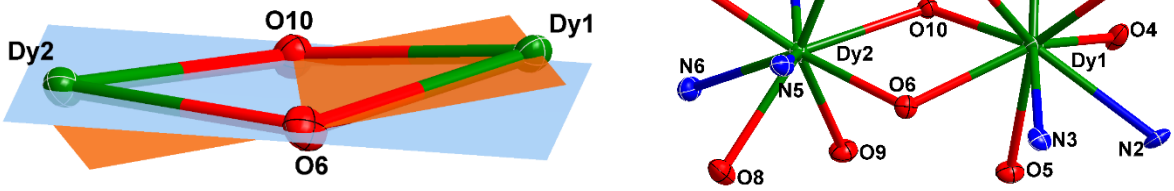

(a) **(b)**

Figure 5. a) Dy_2O_2 core of **1**; b) core structure of **1**. The outer backbone of the ligands are omitted for clarity.

Both the Dy^{III} centers in the complex are nine-coordinate (6O, 3N) in a spherical tricapped trigonal prism geometry as revealed by SHAPE analysis program (Figure 6).[13]

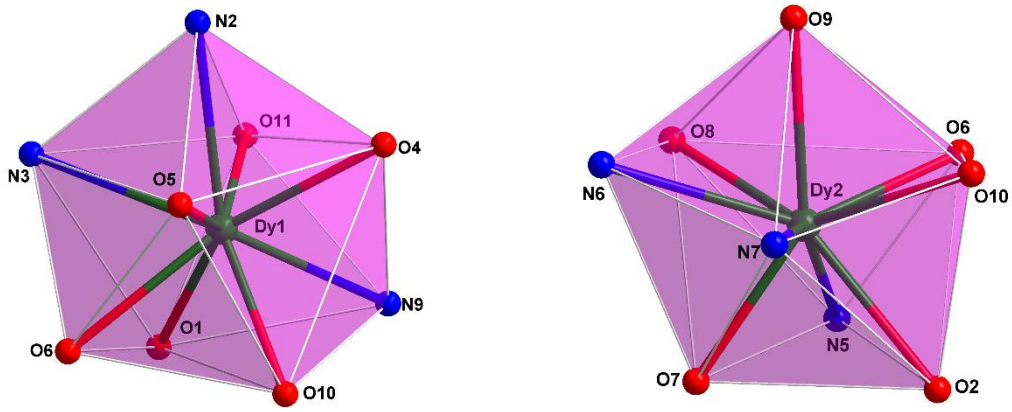

(a) **(b)**

Figure 6. Spherical tricapped trigonal prism coordination geometry around Dy1 (a) and Dy2 (b).

Among all the bond distances the shortest ones are those that involve the phenolate oxygen [Dy1–O11, 2.183(6) Å and Dy2–O7 =2.189(9) Å].

Complex **2** crystallized in the monoclinic, $P2_1/n$ space group. The asymmetric unit, $[Dy_2(LH)(\mu_2\text{-}\ \eta^1\eta^1Piv)(\eta^2\text{-}\ Piv)(OH)]$ comprised of half of the full molecule and consist of one triply deprotonated LH^{3-} ligand, which binds two Dy^{3+} centers along with two pivalate ligands (Figure 7). The neutral tetranuclear assembly is composed of two defective cubes through edge and face sharing (Figure 7). The selected bond angles and bond lengths of the complex are provided in the caption of Figure 7

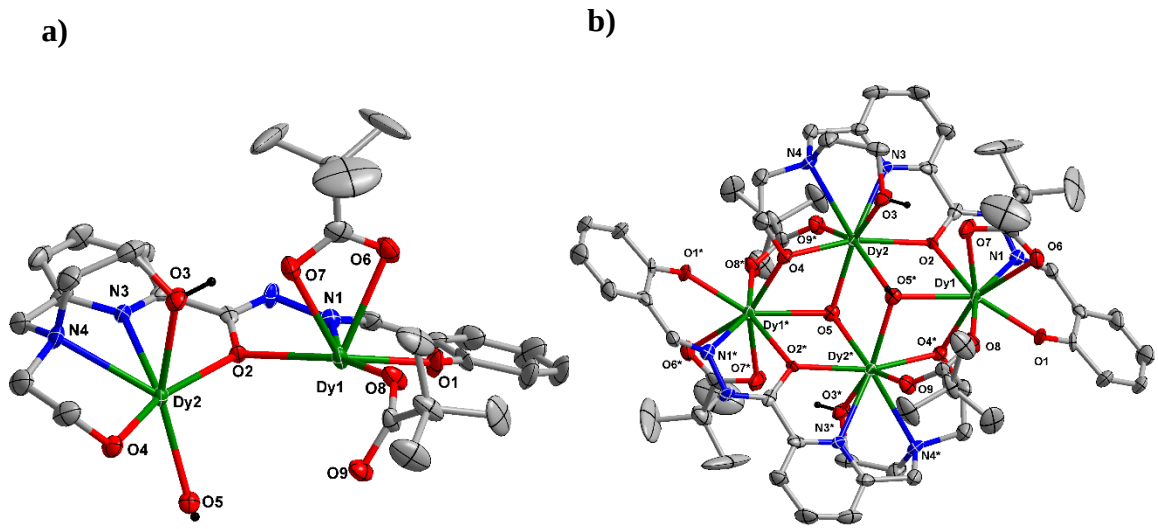

Figure 7. (a) Asymmetric unit of **2**, (b) Molecular structure of **2.** Thermal ellipsoids at 50% probability level are shown (selected hydrogen atoms and the solvent molecules have been omitted for clarity). Color codes: N = blue; O = red; C = grey; Dy= dark green and H = black. Selected bond lengths (Å) for **2**: for Dy1; Dy1–O1, Dy1–O2, Dy1–O4*, Dy1–O5*, Dy1–O6, Dy1–O7, Dy1–O8, Dy1–N1, are 2.231 (5), 2.368(5), 2.280(5), 2.434(4), 2.555(8), 2.432(7), 2.309(6), 2.533(6), respectively, for Dy2; Dy2–O2, Dy2–O3, Dy2–O4, Dy2–O5, Dy2–O5*, Dy2–O9, Dy2–N3, Dy2–N4, are 2.340(5), 2.407(5), 2.424(5), 2.341(5), 2.342(6), 2.313(6), 2.528(7), 2.629 respectively, and selected bond angles for **1**: Dy1–O2–Dy2, Dy1–O5–Dy2, Dy2–O5–Dy1*, Dy2–O4–Dy1*, Dy2–O5–Dy2*, are 113.3(2)°, 111.1(3)°, 101.0(2)°, 109.0 (2)°, 108.0(2)°, respectively.

The proliferation from the dinuclear motif to the tetranuclear complex occurs primarily as a result of the bridging coordination of the de-protonated diethanolamine arms. In addition two μ_3-OH ligands assists in binding three Dy^{III} together. Among the pivalate ligands while one binds in

a chelating anisobidentate manner with one Dy^{3+} [(Dy1–O6=2.555(8) Å, Dy1–O7=2.432(7) Å)] the other functions ~~as a~~ as a bridging ligand (μ_2-η^1:η^1) between two Dy^{III} centers. (Figure 8).

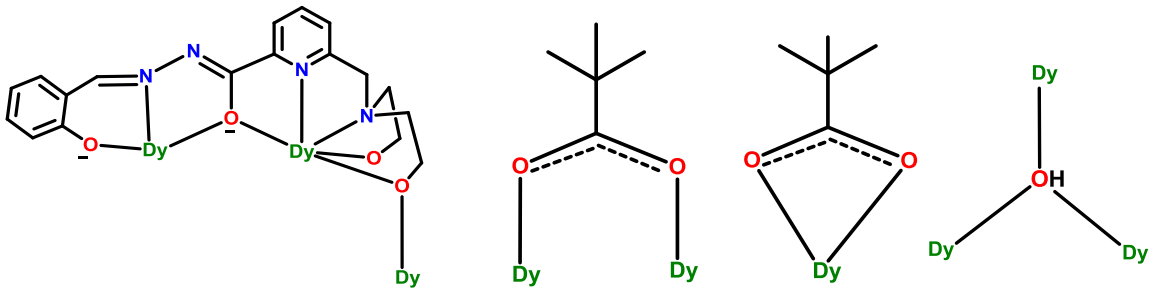

$\mu_3 - \eta^1: \eta^1: \eta^2: \eta^1: \eta^1: \eta^1: \eta^2$ $\mu_2 - \eta^1\ \eta^1$ η^2 μ_3

Figure 8. Ligands coordination modes involved in the tetranuclear assembly**.**

The defect cubane core $[Dy_4(\ \mu_2\text{-}O)_4\ (\mu_3\text{-}dOH)_2]^{6+}$ contains four coplanar metal centres, Dy1, Dy1* and Dy2, Dy2*(Figure 9)

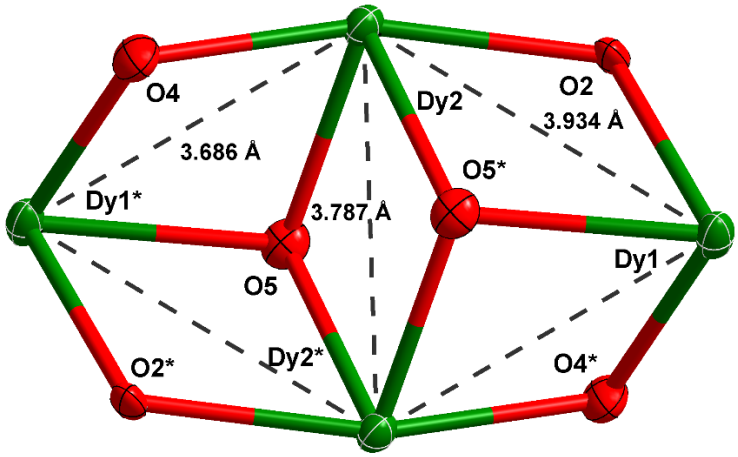

Figure 9. Butterfly shaped tetranuclear core of **2.**

Overall, **2** contains two different types of eight-coordinate Dy^{III} centers; one having a 7O, 1N coordination environment (Dy1) and the other having a 6O, 2N environment (Dy2). Both of these metal centres have been shown to possess a triangular dodecahedron geometry by the SHAPE analysis program (Figure 10).[13]

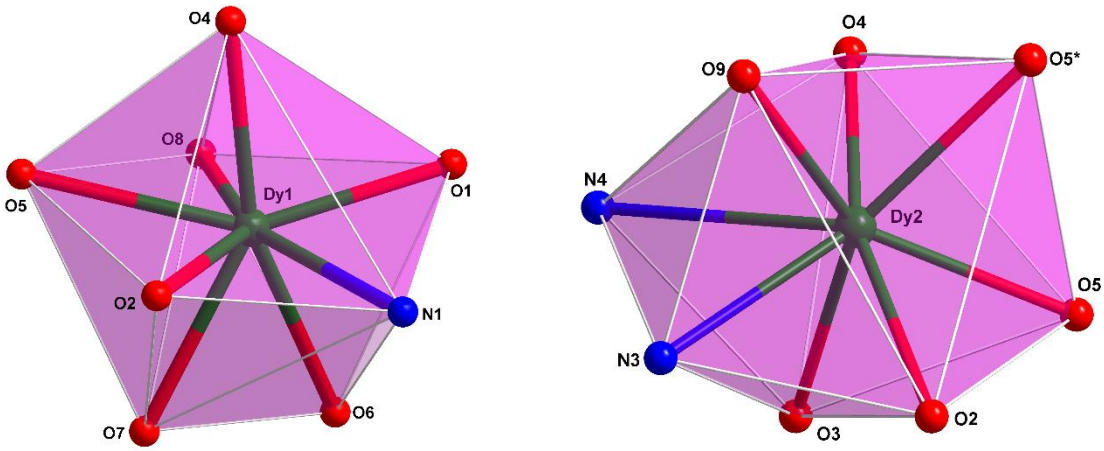

(a) **(b)**

Figure 10. Spherical capped square antiprism coordination geometry around Dy1 (a) and Dy2 (b).

The selected bond parameters are provided in the caption of Figure 7. The Dy–N bonds distances range from 2.528(7) – 2.669(7) Å and the longest bond observed between $Dy–N_{diethanolamine}$ (Dy2–N4=2.629(7). The observed average $Dy–O_{CH2OH}$ bond length is 2.415(5) Å and found slightly longer than $Dy–O_{hydrazone}$ (2.354(5) Å). The average $Dy–O_{piv}$ bond lengths are 2.432(7) Å and

found slightly longer than Dy–$O_{hydrazone}$ bond length. Then shortest distance among the Dy-O distances is found in Dy-O_{phen} (Dy1–O1=2.231(5).

The crystal structure of **2** reveals two pairs of intramolecular hydrogen bonds (O7*-H3*-O3*, O7-H3-O3) and four CH···O interactions leading to the formation of a 2D polymeric structure (Figures S1-S2)

The X-ray diffraction study of **3** reveals that the homometallic hexanuclear complex is cationic with five chloride counter ions (It crystallized in the space group $P2_1/n$ with Z = 4). The asymmetric unit consists of the full molecule, *viz*, $[Dy_6(LH_2)_3(\mu_3–OH)(\mu_3–CO_3)_3(CH_3OH)_4(H_2O)_8]\ 5Cl\cdot 3H_2O$ (Figure 11). The molecular structure of **3** is provided in Figure 11 and selected bond parametres are given in Supporting Information (Table S5).

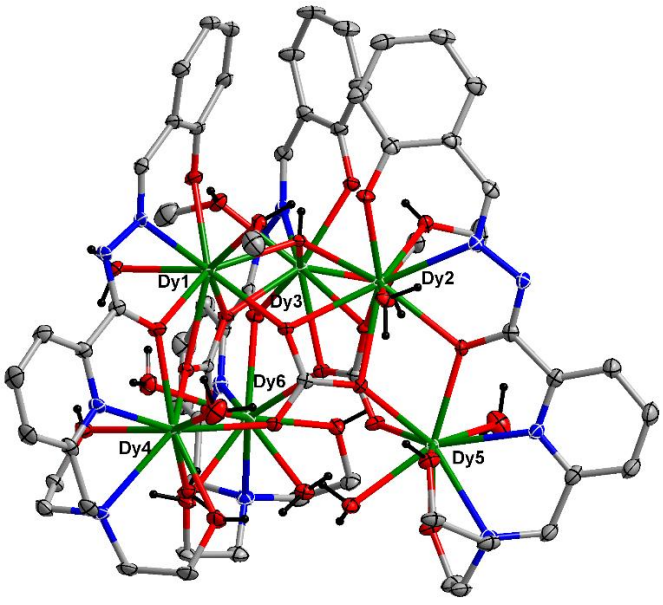

a)

Figure 11. (a) Molecular structure of **3**, (b) Core of **3.** Thermal ellipsoids at 50% probability level are shown (selected hydrogen atoms and the solvent molecules have been omitted for clarity). Color codes: N = blue; O = red; C = grey; Dy= dark green; H = black Some selected shortest bond lengths (Å) for **3** around the metal centres: for Dy1; Dy1–$O1_{phen}$, Dy1–$O2_{enolato}$, Dy1–$O13_{hydroxide}$, Dy1–$O14_{carbonate,}$ Dy1–$O20_{carbonate}$, Dy1–$O22_{carboante}$, are 2.2671(19), 2.3969(19), 2.439(2), 2.3710(19), 2.5017(19), 2.4652(19), respectively, for Dy2; Dy2–$O5_{phen}$, Dy2–$O6_{enolato}$, Dy2–$O13_{hydroxide}$, Dy2–$O14_{carbonate,}$ Dy2–$O16_{carbonate}$, Dy2–$O17_{carboante}$, are 2.2722(19), 2.4078(19), 2.427(2), 2.4992(19), 2.4575(19), 2.3771(19), respectively, for Dy3;

b)

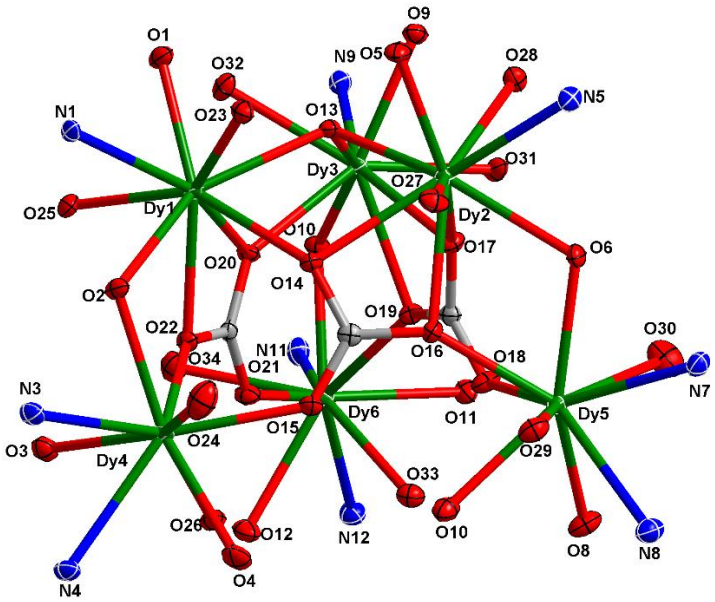

Dy3–$O9_{phen}$, Dy3–$O10_{enolato}$, Dy3–$O13_{hydroxide}$, Dy3–$O17_{carbonate,}$ Dy3–$O19_{carbonate}$, Dy3–$O20_{carbonate}$, are 2.2606(19), 2.4001(19), 2.413(2), 2.4898(19), 2.4705(19), 2.3552(19), respectively, for Dy4; Dy4–$O2_{enolato}$, Dy4–$O15_{carbonate,}$ Dy3–$O22_{carboante}$, are 2.3861(19), 2.3429(19), 2.3467(18), respectively, for Dy5; Dy5–$O6_{enolato}$, Dy5–$O16_{carbonate,}$ Dy5–$O18_{carbonate}$, are 2.3919(19), 2.3407(18), 2.357(2), respectively, for Dy6; Dy6–$O10_{enolato}$, Dy6–$O19_{carbonate}$, Dy6–$O21_{carbonate}$, are 2.3927(19), 2.3571(19), 2.3366(19), respectively.

The hexanuclear assembly **3** consists of three dinuclear sub units (Dy1/Dy4, Dy2/Dy5, Dy3/Dy6), each sub unit being held together by $[LH_2]^2$in μ_2– η^1: η^1: η^2: η^1: η^1: η^1: η^1 fashion (Figure 12).

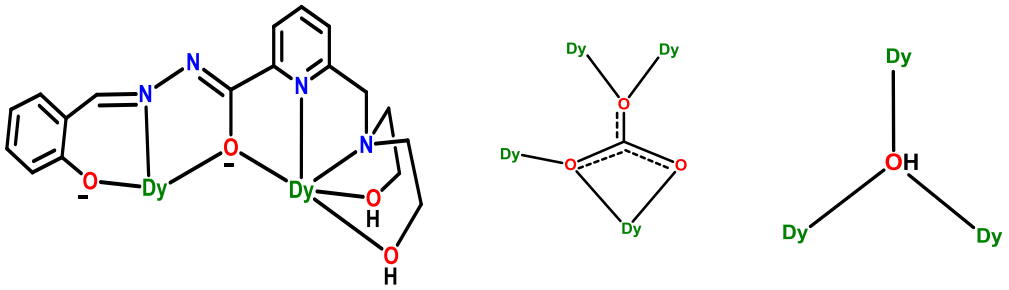

$\mu_2 - \eta^1: \eta^1: \eta^2: \eta^1: \eta^1: \eta^1: \eta^1$ $\mu_4 - \eta^1\ \eta^2\ \eta^2$ μ_3

Figure 12. Ligands coordination modes involved in the tetranuclear assembly**.**

Three such dinuclear subunits are stitched together by three carbonate ligands in a μ_4 -η^1:η^2:η^2 fashion and one $[\mu_3\text{-OH}]^-$ to afford a propeller-shaped hexanuclear assembly(Figure 13).

a)

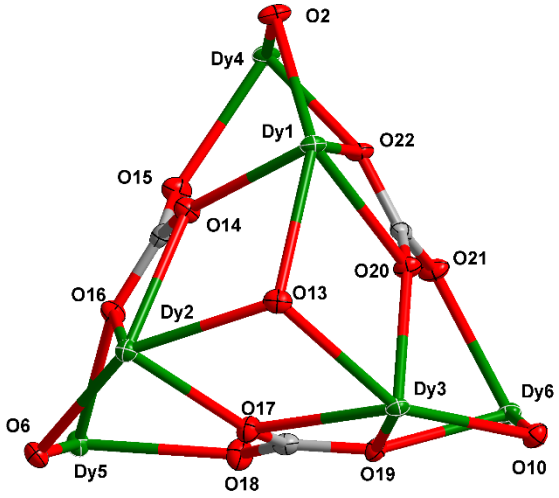

b)

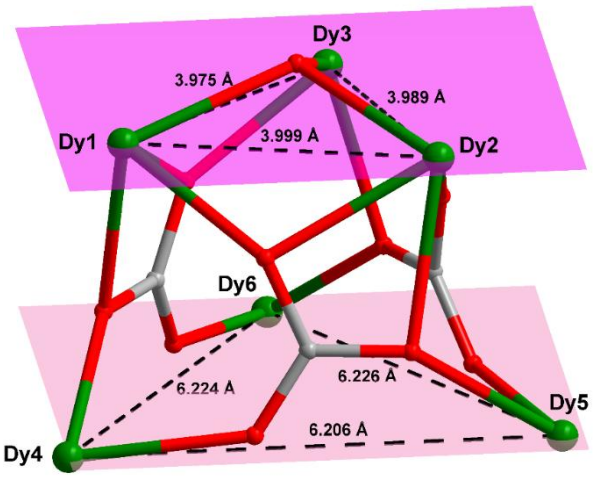

Figure 13. a) View of propeller shaped Dy_6 core; b) View of the Dy_6 central core in two isosceles triangles in **3**.

The metal coentres in the hexanuclear assembly are at the corners of two isosceles triangles [$d_{Dy1\text{-}Dy2}$ =3.999 Å, $d_{Dy2\text{-}Dy3}$ =3.989 Å, $d_{Dy1\text{-}Dy3}$ =3.975 Å and Dy4/Dy5/Dy6 where $d_{Dy4\text{-}Dy5}$ =6.206 Å, $d_{Dy5\text{-}Dy6}$ = 6.226 Å, $d_{Dy6\text{-}Dy4}$ =6.224 Å] (Figure 13b).

All the Dy^{III} centres are nine-coordinate. Three of these, Dy4, Dy5 and Dy6 have a 2N, 7O coordination environment while Dy1, Dy2 and Dy3 have a 1N, 8O coordination environment in a Muffin shape as determined by the SHAPE analysis program (Figure 14).[13]

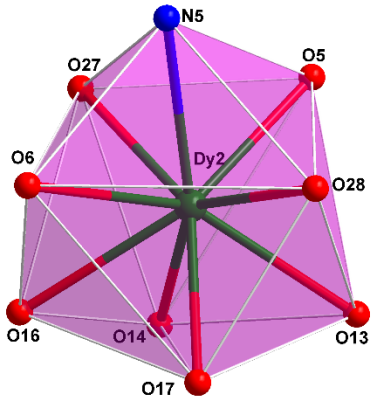

(a)

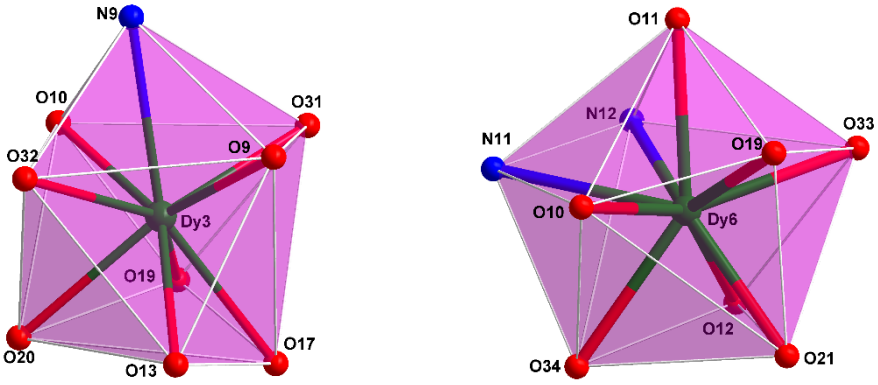

(b) (c)

Figure 14. Spherical capped square antiprism geometry (Muffin shape) in (a) Dy2, (b) Dy3 and (c) Dy6.

As in the other complexes the shortest Dy-O distance is observed for the coordination involving the phenolate oxygen atom. Some selected bond parameters are given in the caption of Figure 11 and Table S5.

Magnetic Properties

The temperature dependence of the magnetic susceptibility for **1-3** in the 2-300 K range and under a constant magnetic field of 0.1 T is shown in Figure 15. At room temperature the $\chi_M T$ values for **1-3** of 28.80, 56.90 and 83.70 $cm^3 \cdot mol^{-1} \cdot K$, respectively, are close to the expected values of 28.34, 56.7 and 85.02 $cm^3 \cdot mol^{-1} \cdot K$ for two, four and six Dy^{3+} ions respectively, in the free-ion approximation (J =15/2 and g = 4/3). When lowering the temperature, the $\chi_M T$ product for **1-3** remains nearly constant from room temperature to approximately 40 K, 45 K and 70 K, respectively, whereupon it starts to decrease in a ~~more~~ deeper manner reaching minimum values of 26.02, 32.94 and 50.29 $cm^3 \cdot mol^{-1} \cdot K$, respectively, at 2 K. This decrease could be attributed to the thermal depopulation of the Kramers doublets arising from the splitting the ground multiplet

by crystal field effects and to the ~~existence of~~ possible existence of intramolecular antiferromagnetic interactions between the Dy^{3+} ions.

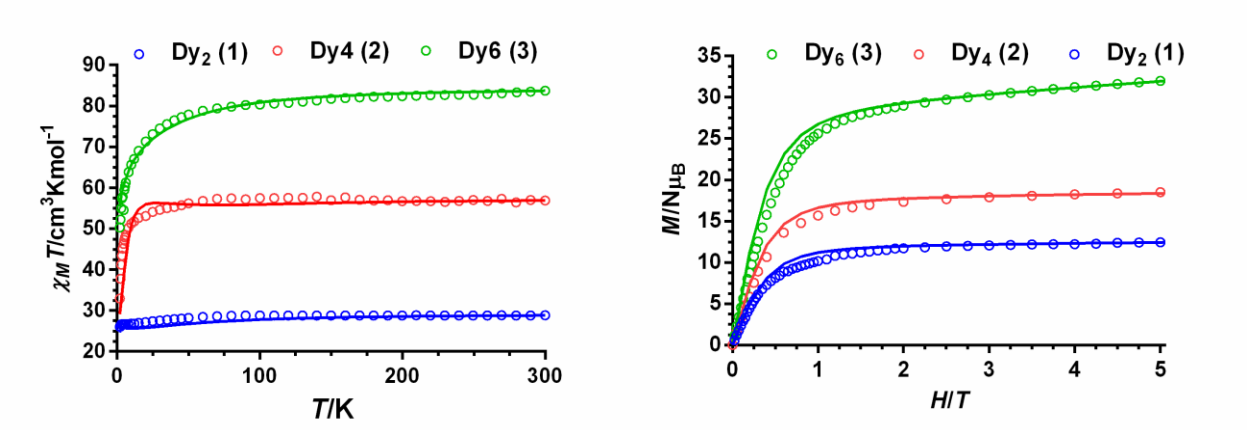

Figure 15. Temperature dependence of $\chi_M T$ (left) and field dependence of the magnetization (right) for complexes **1**-**3**. Solid lines represent Poly_aniso fitted molar magnetic susceptibility vs. T and M vs. H curve.

The isothermal magnetization curves measured at 2 K and up to 5 T for complexes **1**-**3** (Figure 15 right) show a relatively rapid increase in the magnetization at low field and a quasi linear increase at high field without achieving a complete saturation at 5T (complex **1** and **2**, however, ~~is~~ are almost magnetically saturated at 5 T). This behaviour suggests the presence of a significant magnetic anisotropy and/or the presence of low-lying excited states that are partially populated at this temperature. The low-lying excited states are in agreement with weak magnetic interactions expected for these systems. It is worth noting that even though the $\chi_M T$ vs. T plot does not show a maximum at very low temperature and the M vs. H plot does not display a S-shape, the second derivative of $\chi_M T$ vs. T plot and the first derivative of M vs. H (see Figure S3), might be

cautiously indicative of a non-magnetic ground state, whose more patent effects should be observed below 2 K.

The magnetization values at the maximum applied field of 5 T are rather lower than expected for the free ion approximation (10, 20 and 40 Nβ for **1**-**3**, respectively), which supports the presence of significant magnetic anisotropy due to crystal-field splitting effects.[6e,14,15]

It is worth noting that the χ_M'T product (χ_M' is the in-phase ac susceptibility, Figure S4) for **1** at low temperature, where all the lines are coincident, is 23.0 cm^3mol^{-1} K, which is not too far from that expected for randomly oriented crystals with a $M_J = \pm 15/2$ Ising ground Kramers doublet (25 cm^3 mol^{-1} K). This fact is not unexpected as Dy^{III} complexes with a non-symmetric coordination environment, like **1**, generally exhibit an axial ground state (details are provided in the theoretical studies). For instance, Dy^{III} complexes with a Dy-O bond distance significantly shorter than the other Dy-donor distances possess an axial ground state with the anisotropic magnetic moment oriented along the shortest Dy-O direction.[15] This orientation can be easily understood taken into account that the *f* electron density of the $M_J = \pm 15/2$ Dy^{III} sublevels has an oblate shape. Because of this and to reduce the repulsion with the closest coordinated ligand donor atom (usually that possessing the largest electron density), the *f* electron density disc is accommodated almost perpendicular to the shortest Dy-O bond and then the magnetic moment is placed along this bond direction. This is the case of **1**, where the sole crystallographically independent Dy^{III} ion shows a Dy-$O_{phenoxide}$ bond distance of 2.190 Å, which is rather shorter than the other ones in the 2.323-2.607 Å range. We have calculated the direction of the anisotropy axes of the Dy^{III} ions by using the electrostatic Chilton's method and the Magellan software[16] and, as expected, the results show that the anisotropy axis on the two-fold symmetrically related Dy^{III} ions is located close to the Dy-$O_{phenoxide}$ bond (Figure S5), with an

angle between their respective directions of 10.98°. The angle between the anisotropic axis and the molecular plane is 32.84 º, whereas the angle between the line connecting the Dy^{III} ions and the anisotropy axis is 60.8º.

It is worth noting that the main contribution to the magnetic coupling in oxo-bridged dinuclear Dy^{III} complexes with short Dy···Dy distances of approximately 3.9 Å generally arises from the magnetic dipolar coupling rather than from exchange coupling. The dipolar contribution to the magnetic coupling can be calculated by the following equation for the energy of the dipole-dipole interaction:[15]

$$E_{dip} = -\left\{\frac{\mu_0}{4\pi}\right\}\frac{1}{r_{ij}^3}\left[3(\vec{\mu}_i \cdot \vec{u}_{ij})\vec{u}_{ij} - \vec{\mu}_i\right] \cdot \vec{\mu}_j$$

equation 1

where u_{ij} is the unit vector connecting the interacting centres i and j and *r* is their distance, $\mu_{i,}$ and $\mu_{j,}$ are the magnetic moments of centers *i* and *j* and μ_0 is the vacuum permittivity. This expression leads to antiferromagnetic coupling for angles between the magnetic moments and the molecular plane (θ) bigger than 66.73° and ferromagnetic coupling for angles lower than this value, respectively (for an angle value of 62.09° between the magnetic moments *i* and *j*, while the threshold angle value for a collinear system is 54.7°). In the case of **1**, the angle between the local magnetic moments of the ground state and the molecular plane (of 33.4º) (see Figure S5) determines the positive sign of the magnetic dipolar interaction. The estimated value of J_{dip} from equation **1** with the Hamiltonian $H_{dip} = -J_{dip}J_{z1}J_{z2}$ (where $J_{z1}J_{z2}$ represent the M_J values of the ground doublet state of the i and j centers) is +0.019 cm^{-1}. In good accordance with this, the $\chi_M T$ of **1** below 10 K is almost constant with a value of 26.5 $cm^3mol^{-1}K$ (only shows a slight decrease

below 2.5 K ~~that can be due to intermolecular interactions~~, Figure S6), which could be indicative of the existence of very weak ferromagnetic interaction between the Dy^{III} ions. Thus, below 10 K, this very weak dipolar ferromagnetic interaction could balance the decrease in $\chi_M T$ due to the depopulation of the M_J sublevels, so that the $\chi_M T$ would remain almost constant. The existence of a very weak magnetic interaction is not unexpected because the 4 *f* orbitals of the Dy^{III} are deeply buried into the atom and then very well shielded from the ligands by the 5p and 6s orbitals, so that they have very little overlap with the bridging enolate oxygen atoms.

Several examples of dinuclear Dy_2 complexes containing hydrazine-enolate mulidentate bridging ligands, like that acting in **1**, have been reported so far.[17] In these complexes the two enolate oxygen atoms bridge the Dy^{III} centers to afford a rhombic $Dy(O)_2Dy$ bridging fragment (Table 2). All these complexes present similar Dy-O, Dy-O-Dy and Dy···Dy parameters in the bridging region with almost equal Dy-O distances within the $Dy(O)_2Dy$ fragment, and, with the exception of $[Dy_2(NO_3)_4(L_3)_2MeOH]$, exhibit ferromagnetic coupling. Although there is no a clear correlation between the sign of the magnetic coupling and the values of the bridging parameters, however, it seems that the combination of larger values of Dy-O, Dy-O-Dy and Dy···Dy parameters in the bridging may favour weaker ferromagnetic interactions or even antiferromagnetic interactions. Thus, the complex $[Dy_2(NO_3)_3(L_4)_2MeOH]$ showing the greatest Dy-O, Dy-O-Dy and Dy···Dy values, presumably exhibits very weak antiferromagnetic interaction. Nevertheless, because the contribution to the magnetic coupling arisig from the dipolar magnetic interactions in this type of Dy_2 complexes with Dy···Dy distances between 3.8 Å and 4 Å is rather larger than the magnetic exchange interaction, the Dy···Dy distance plays a more relevant role than the other bridging parameters. It is worth noting that, in good accord with the above equation, when there is a near- parallel alignment of the local anisotropy axes and the

line connecting the dysprosium ions ($\theta = 0$) relatively stronger ferromagnetic dipolar interactions are expected. This is the case of complexes $[Dy_2(NO_3)_2(L_1)_2(H_2O)_2]\cdot 2H_2O$,[17a] $[Dy_2(NO_3)_2(L_2)_2(CH_3OH)_2]\cdot 4CH_3CN$, [17b] $[Dy_2Cl_2(H_2L_1)_2(MeOH)_3]\cdot CH_3CN$,[7a] where the two shortest Dy-O distances are those corresponding to the phenoxido oxygen atoms coordinated almost in *trans* positions to the line connecting the Dy^{III} ions. In such a disposition, the anisotropy axes align to the Dy-$O_{phenoxo}$ direction, which is near parallel with the line connecting the Dy^{III} centres. In the case of $[Dy_2(NO_3)_4(L_3)_2MeOH]$,[17c] however, the Dy-O distances are found in the 2.326-2.586Å range, so that the distribution of the charged oxygen atoms is rather spherical. In this case, the calculation of the orientation of the anisotropic axes using the Magellan program may be meaningless. Keeping it in mind, the results of the calculation indicate that the anisotropic axes are almost perpendicular to each other, which, together with the large Dy···Dy distance, would led to a ferromagnetic interaction much weaker than observed in the other three complexes gathered in Table 2.

Table 2.- Structural parameters in the Dy_2O_2 bridging core and nature of the magnetic interactions for some dinuclear Dy^{III} complexes containing hydrazine-enolate mulidentate bridging ligands.

Complex	Magnetic Interaction	Dy···Dy (Å)	Dy-O (Å)	O-Dy-O (º)	Coord. Sphere	Ref.
$[Dy_2(NO_3)_2(L_1)_2(H_2O)_2]\cdot 2H_2O$	F	3.8258	2.348 2.319	110.1	N_2O_6	17a
$[Dy_2(NO_3)_2(L_2)_2(CH_3OH$	F	3.9225	2.319 2.313	114.9	N_2O_6	17b

$)_2]\cdot 4CH_3CN$						
$[Dy_2Cl_2(H_2L_1)_2(MeOH)_3]\cdot CH_3CN$	F	3.8644	2.334 2.335 2.322 2.310	112.3 111.5	$N_2O_3Cl_2$ N_2O_6	7a
$[Dy_2 (NO_3)_4(L_3)_2MeOH]$	___	3.945	2.359 2.364	114.7 113.7	N_4O_6 N_2O_7	17c
$[Dy_2 (\mu\text{-}NO_3)_2(H_2L)_2]\cdot[NO_3]\cdot 2H_2O$	___	3.976	2.323[a] 2.503[a]	110.66	N_3O_6	This work

[a].average values. H_2L1: pyridine-2-carboxylic acid [(2-hydroxy-3-methoxyphenyl)methylene] hydrazide; L2: N'-2-((2-hydroxy-1-naphtyl)methylene)picolinohydrazide; L3: N'-(1-(pyridin-2-yl)ethylidene)pyridine-2-carbohydrazide; H_4L: 6-((bis(2-hydroxyethyl)amino)-*N´*-(2-hydroxybenzylidene)picolinohydrazide

Compared to these four complexes, complex **1** presents the following important differences: (i) The Dy-O distances within the Dy(μ-O_2)Dy bridging fragment are rather different and, moreover, one of them (of ~2.5 Å) is rather long. This further leads to a Dy···Dy distance that is larger than those observed in the other complexes given in Table 2, (ii) the anisotropic axes are not parallel to each other and with the line connecting the Dy^{III} centrers. (iii) There exists an additional nitrate ligand bridging the Dy^{III} ions in a μ_2- η^1:η^1 fashion. The nitrate bridging ligand is known to transmit very poor magnetic interactions in transition metal complexes [18] and, therefore, much weaker interactions are expected in Dy^{3+} nitrate bridged complexes. In view of this, we will assume that the role played by the multiatomic nitrate bridge in transmitting

magnetic exchange interaction compared to the monoatomic enolate bridges, if any, is negligible. As for the differences (i) and (ii), both would reduce the magnitude of the exchange and dipolar contributions to the ferromagnetic coupling with regard to those expected for complexes $[Dy_2(NO_3)_2(L_1)_2(H_2O)_2]\cdot 2H_2O$, $[Dy_2(NO_3)_2(L_2)_2(CH_3OH)_2]\cdot 4CH_3CN$, $[Dy_2Cl_2(H_2L_1)_2(MeOH)_3]\cdot CH_3CN$, which is in good accordance with the experimental results. Nevertheless, these conclusions ~~drawn~~ about the nature and magnitude of the magnetic coupling in this type of alkoxide bridged Dy_2 complexes should be taken with caution, as other factors such as the type and distributions of donor atoms in the Dy^{III} coordination sphere are likely to affect magnetic coupling between the Dy^{III} ions.

In view of the above considerations for complex **1**, it is clear that the magnetic coupling between the Dy^{III} ions is very weak and hence the magnetic behaviour should be single-ion in origin. Moreover, as indicated above, the short Dy-$O_{phenoxo}$ distance anticipates an axial anisotropy of the ground state of the Dy^{III} ion in **1**.[15] Consequently, it is probable that this compound exhibits slow relaxation of the magnetization and SMM behaviour at zero magnetic field. In order to verify this, alternating current *ac* magnetic susceptibility measurements as a function of the temperature and frequency were performed on complex **1**. The results show frequency dependent maxima in the χ_M'' signals below 10 K (see Figure 16) that overlap with a tail at low temperature (χ''_M does not go to zero below the maxima but increases up to 2 K at low frequencies), thus confirming the existence of slow relaxation and SMM behavior at zero-field.

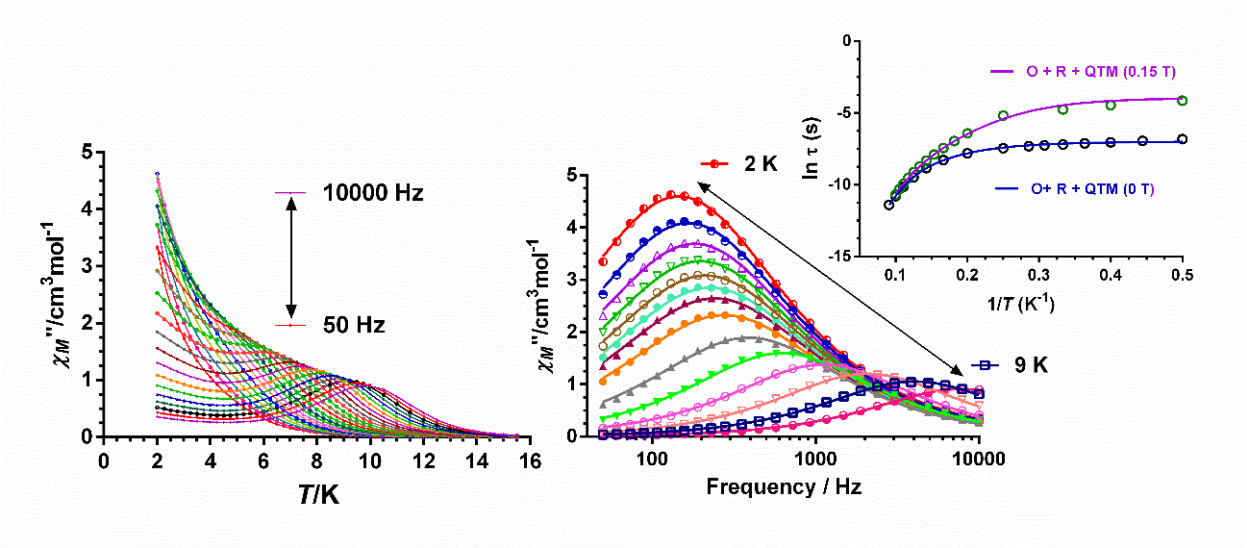

Figure 16. Temperature and frequency dependence of the out-of-phase χ_M'' susceptibility signals for complex **1** under zero field. The solid lines in the figure on the right side represent the best fit to the generalized Debye model. Inset: Arrhenius plot for the relaxation times. Solid lines account for the best fits considering the simultaneous presence of Orbach + Raman + QTM relaxation processes at zero (blue) and 1500 Oe (purple) applied fields.

This appearance of this tail suggests the existence of fast quantum tunneling of magnetization (QTM) at very low temperature, which can arise from transverse anisotropy in the ground state, and from the transversal field created by dipole-dipole and hyperfine interactions. The Cole-Cole diagram for **1** under zero field in the temperature range 2-10 K (Figure S7) exhibits semicircular shapes with α values in the range 0.18 (2 K)-0.06 (10 K), thus suggesting the existence of a relatively narrow distribution of relaxation processes. Below 5 K, both QTM and Raman could contribute to the magnetization relaxation (the field dependence of the relaxation time rules out the existence of direct process), whereas above 5 K only Raman and Orbach relaxation processes could be operative.

The values of the relaxation times (τ) at each temperature were extracted from the fitting of the frequency dependence of χ''_M at different temperatures to the generalized Debye model. The temperature dependence of the relaxation times in the form of an Arrhenius plot (Figure 16 insert) shows, apart from the lineal portion in the high temperature range (representative of a thermally activated process), a curvature for the intermediate temperatures and almost constant relaxation times below 3 K, this latter being indicative of QTM. Therefore, the relaxation times were fitted to the following equation:

$$\tau^{-1} = BT^{n} + \tau_0^{-1} exp(-U_{eff}/k_B T) + \tau_{QTM}^{-1} \qquad \textit{equation 2}$$

which takes into account the simultaneous presence of Raman, Orbach and QTM relaxation modes, respectively. The best fit afforded the following parameters: B = 2.4(9) $s^{-1}K^{-3.9}$, n = 3.9; $\tau_0 = 6.4(3)\cdot 10^{-9}$ s, U_{eff} = 87(1) K and τ_{QTM} = 0.0004(1) s. Although a value of 9 is expected for Kramers ions like Dy^{III}, however, when both acoustic and optical phonons are present, values between 2 and 7 can be considered as reasonable.[19]

In order to fully or partly remove the QTM relaxation process, *ac* measurements on compound **1** were performed in the presence of an optimal small external dc field of 0.15 T (that inducing the slowest relaxation process). The value of the optimal field was extracted from field dependence of the relaxation time at 3 K (see Figure S8). Under the optimal field the low tail due to QTM relaxation has not been fully eliminated and/or an incipient field-induced relaxation process appears below 3.5 K (Figure S9). In good accordance with the latter suggestion and the existence of multiple processes, α values below 4 K are greater than the extracted ones under zero-applied magnetic field at the same temperatures (Figure S10). Nevertheless, temperature and frequency dependent well-defined maxima between 5 K (50 Hz) and 10 K (10000 Hz) appeared for all the used frequencies (Figure S9). The Cole-Cole diagram for **1** under an applied field of 0.15 T in

the temperature range 5-9 K (Figure S10) exhibits semicircular shapes with α values in the range 0.18 (5 K)-0.08 (9 K), thus suggesting the existence of a relatively narrow distribution of relaxation processes.

The relaxation times, extracted from the fitting of the frequency dependence of χ_M" at different temperatures to the Debye model, are plotted in the form of lnτ vs 1/T in Figure 16 inset. As it can be observed in this figure, apart from the linear region in the high temperature range of the plot, a remarkable curvature appears for the intermediate and low temperature regions, suggesting the presence of multiple relaxation processes. In view of this, the relaxation times were also fitted to the equation 2. The best fitting led to the following parameters: B = 0.08(2) $s^{-1}K^{-5.5}$, n = 5.5; $\tau_0 = 2.5(1)\cdot10^{-9}$ s, U_{eff} = 101(3) K and τ_{QTM} = 0.02(1) s. As expected, the applied magnetic field induces a partial quenching of QTM and then a slowdown of this relaxation process, together with a concomitant increase of U_{eff}.

Dynamic ac measurements of complex **2** under zero field show frequency and temperature dependence of both in-phase (χ'_M) and out-of-phase (χ''_M) signals below 15 K, which can be indicative of slow relaxation of the magnetization and SMM behavior (Figure 17 and Figure S11). The χ''_M vs T plot at frequencies in the 50-1000 Hz range (Figure S11) displays a broad signal with incipient maxima around 9 K, which overlap with a high intensity tail appearing at lower temperatures. Below 6000 Hz, maxima becomes shoulder of the low temperature tail and finally disappear, so that at low frequencies the χ''_M component steadily increases below 15 K (Figure S11). This behavior can be attributed to overlapping of different relaxation processes, including a fast quantum tunneling relaxation.

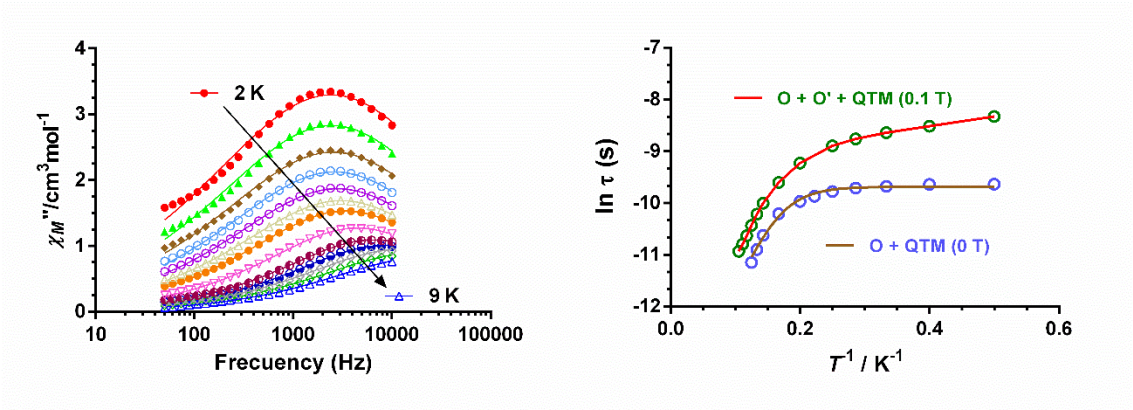

Figure 17. (Left) Frequency dependence of the out-of-phase χ_M" susceptibility signals at different temperatures for complex **2** under zero field (left). The solid lines represent the best fit to the Debye model. (Right) Arrhenius plot for the relaxation times at 0 T (blue circles) and 0.1 T (green cicles) . Solid lines account for the best fits considering the simultaneous presence of QTM + Orbach and QTM + two Orbach relaxation processes at zero (brown) and 0.1 T (red) applied fields, respectively.

The latter process would be responsible for the increase of χ''_M below 4 K. In order to know whether or not this compound shows QTM, we have performed a study of the field dependence of the χ''_M vs frequency plot at 3 K (Figure S12). The results show that the relaxation time for low temperature process increases with the increase of the magnetic field until 0.1 T and then remain constant (Figure S12). Therefore, at least in part, the tail at low temperature should be due to fast QTM. The χ''_M vs f plot at zero field only displays wide maxima in the 1000-10000Hz region (Figure 17). These data were fitted to the generalized Debye model to extract the temperature dependence of the relaxation times (Figure 17 right), which shows the lineal portion in the high temperature region due to a thermally activated Orbach process, a curvature at intermediate temperatures and almost constant relaxation times below 3.5 K (Figure 17 right,

insert). The low temperature behaviour points out the presence of QTM. Taking this into account, the ac data at zero applied dc field were fitted to the following equation:

$$\tau^{-1} = \tau_0^{-1} exp(-U_{eff}/k_B T) + \tau_{QTM}^{-1} \qquad \textit{equation 3}$$

where the first term corresponds to an Orbach process and the second one to QTM. The best fit afforded the following parameters: $\tau_0 = 4.2(1)\cdot10^{-7}$ s, $U_{eff} = 31(2)$ K and $\tau_{QTM} = 0.000062(1)$ s.

In order to try to eliminate at least partly QTM, ac measurements were carried out under the optimal dc field of 0.1 T. The results indicate that the χ''_M vs T plot has not been essentially modified with respect to that observed at zero dc field (Figure S13). Therefore, either QTM has been weakly quenched or the tail at low temperature is not due to QTM but to a thermally activated process with so small effective thermal energy barrier (*Ueff*) that its maxima appear below 2 K. As expected, the χ''_M vs f and the temperature dependence of the relaxation times plots under 0.1 T are very similar to those observed under zero dc field (Figure S14 and Figure 17 right). The temperature dependence of the relaxation times at 0.1 T were fitted to equation 3, which implies the assumption of the existence of Orbach and QTM processes. The best fitting procedure led to the following parameters: $\tau_0 = 9(1)\cdot10^{-7}$ s, $U_{eff} = 28.8$ (9) K and $\tau_{QTM} = 0.00017(1)$ s. Although the parameters are very similar to those extracted under zero-field, however, QTM is rather smaller, as expected. In this scenario, the thermally activated process should contain the relaxation processes arising from the two different crystallographic independent Dy^{III} centers and the exchange interaction between them should favour the QTM process, which is not eliminated even in the presence of an applied magnetic field. An alternative scenario would be that of considering that the intense tail at low temperature is due to a thermally activated process and so the temperature dependence of the relaxation times was fitted to the following equation:

$$\tau^{-1} = \tau_{01}^{-1} exp(-U_{eff1}/k_BT) + \tau_{01}^{-1} exp(-U_{eff12}/k_BT) + \tau_{QTM}^{-1} \quad \textit{equation 4}$$

where the first and second terms represent two different thermally activated processes and the third term the remaining QTM. The best fit allowed extracting the following parameters: τ_{01} = 2(1)·10^{-7} s, U_{eff1} = 37(8) K, τ_{02} = 5(6)·10^{-5} s, U_{eff2} = 8(4) K and τ_{QTM} = 0.000067(9) s. In this latter scenario, the low and high temperature overlapping processes appearing in the χ''_M vs T plot could be assigned to each ~~of the~~ type of Dy^{III} ions that are present in the structure, Dy1 and Dy2, with DyNO7 and DyO6N2 coordination spheres. These Dy^{III} ions are rather different, not only due to their distinct coordination spheres, but, and most important, to the number and distribution of the shortest Dy-O distances (< 2.3 Å). Thus, Dy1 has two shortest Dy-O distances, which implicate the phenoxide and one alkoxide oxygen atoms belonging to two different ligands, of 2.229 and 2.283 Å, respectively, which form an angle of 83.71 Å. However, Dy2 only has one shortest Dy-O distance of 2.224 Å involving the alkoxide oxygen atom bridging Dy1 and Dy2. This situation, which similar to that found in complex **1**, is more favorable for the existence of an axial ground state than the disposition observed in Dy1, where the shortest Dy-O distances form almost a right angle. In light of this, Dy1 and Dy2 could be tentatively assigned to the lower and higher temperature processes, with small and high U_{eff} values, respectively.

It is worth mentioning that even though both interpretations of the ac data at 0.1 T for **2** appear to be reasonable, we feel, taking into account also the *ac* results for complex **3** (see below), that the second interpretation (two Orbach plus QTM) could be the most probable to occur.

Dynamic ac measurements of compound **3** at zero applied field indicate that χ'_M and out-of-phase χ''_M components of the susceptibility are frequency and temperature dependent below 15 K (Figure 18 and Figure S15).

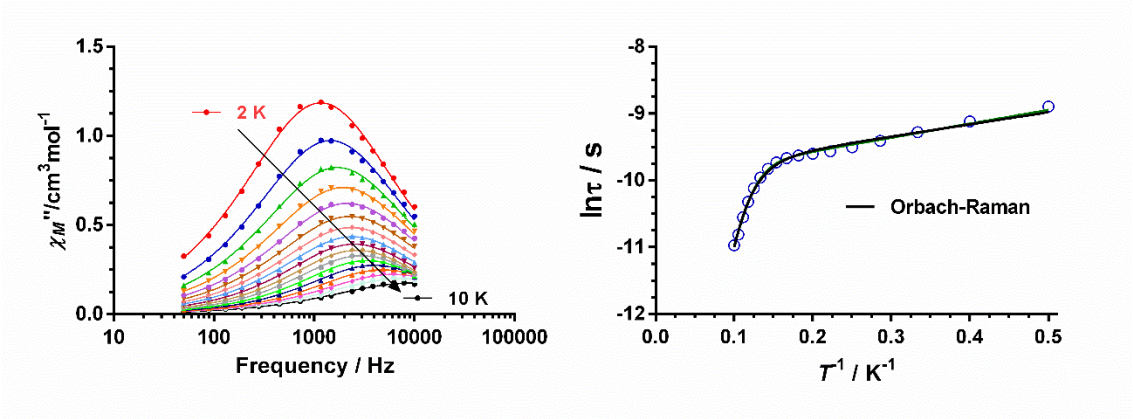

Figure 18.- (Left) Frequency dependence of the out-of-phase χ_M'' susceptibility signals at different temperatures for complex **3** under zero field (left). The solid lines represent the best fit to the generalized Debye model. (Right) Arrhenius plot for the relaxation times at 0 T (blue circles). The black solid line account for the best fits considering the simultaneous presence of Orbach + Raman relaxation processes ~~at zero~~.

In this case, two clear maxima can be observed at ~ 4 K and ~ 10 K above 4000 Hz, indicating the existence of two well differentiated relaxation processes (Figure S15). Nevertheless, below that frequency both processes overlap and no maxima can be observed. The absence of maxima at low frequency and low temperature could be due to QTM and/or a thermally relaxation process with maxima appearing below 2 K. The field dependence of the relaxation times (Figure S16) clearly show that, at very low magnetic fields, relaxation times do not increase with the field as it would be expected if QTM were quenched and, therefore, QTM at zero-field, if any, must be very weak. However, above 0.1 T relaxation times sharply decrease, which could be due

to a field-induced direct relaxation process, which depends on H^4. It should be noted that the frequency dependence of χ''_M as well as the Cole-Cole plot at different temperatures (Figures 18 and S17) only show one relaxation process that must cover the two overlapping processes appearing in the χ''_M vs T plot. In view of this, the χ''_M vs f data at different temperatures were fitted to the generalized Debye model to extract the temperature dependence of the relaxation times for the sole observed process. These data were in turn fitted to equation 2 for a combination of Raman and Orbach processes, so without considering the QTM term. The best fit led to the following parameters B = 0.01(1) $s^{-1}K^{-6.6}$, n = 6.6(4); $\tau_0 = 5(3)\cdot10^{-5}$ s and U_{eff} = 1.8(3) K ~~and τ_{QTM} = 0.02(1) s~~. These parameters should correspond to the average of the two overlapping processes observed in χ''_M vs T plot. Likewise, and to take into account that the low temperature relaxation process could be due to an Orbach type relaxation process, the temperature dependence of the relaxation times was fitted to a sum of two Orbach processes (Equation 4 without considering the third term), leading to the following parameters: $\tau_{01} = 4.6(3)\cdot10^{-8}$ s, U_{eff1} = 62(3) K, $\tau_{02} = 4(6)\cdot10^{-5}$ s, U_{eff2} = 2(1) K. In both scenarios, the low temperature relaxation process exhibits, as expected, a very low value of U_{eff}.

It is worth mentioning at this point that the field induced direct relaxation process (see above) presents its higher intensity at 1900 Oe. Therefore, ac measurements were recorded under this magnetic field, which clearly show in the χ''_M vs T and χ''_M vs f plots the presence of two set of maxima in the 2.5 K (50 Hz)-3.5 K (10000 Hz) and 7.5 K (3000 Hz)-9.5 K (10000 Hz) ranges (Figures S18 and S19). In the χ''_M vs T plot (Figure S18), below 3000 Hz the later peaks overlap with those in the low temperature region, so that no clear maxima are observed in the high temperature region. The Cole-Cole plot clearly exhibits the two relaxation processes and therefore these data were fitted to the sum of two independent processes using the CCFIT

software,[20] allowing extracting the temperature dependence of the relaxation times for the fast (FR) and the slow (SR) relaxation processes (Figure 19). The extracted τ vs T data for the FR process were fitted to a combination of direct and Orbach processes (equation 5):

$$\tau^{-1} = AT + \tau_0^{-1} exp(-U_{eff}/k_B T) \qquad \textit{equation 5}$$

where the first term corresponds to the direct relaxation process. The best fit afforded the following parameters: A = 4(2)·10^3 s^{-1}K, τ_0 = 3.2(2)·10^{-7} s and U_{eff} = 14.6(8) K. It should be noted that the fits to Raman plus Orbach, Raman plus direct and even only Raman processes were rather worse than the Orbach plus direct processes.

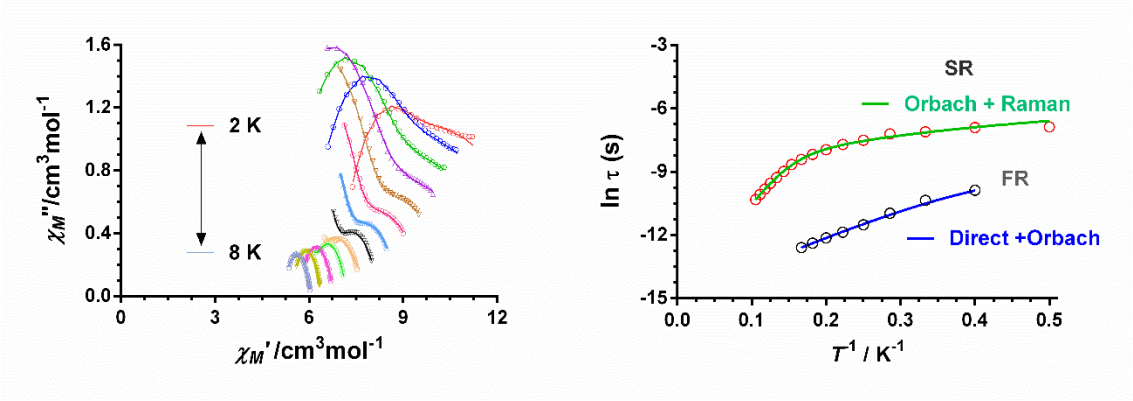

Figure 19.- (Left) Cole-Cole plot for **3** under an applied field of 1900 Oe in the 2-8 K temperature range. Solid lines represent the best fits to the generalized Debye model. (Right) Arrhenius plot for the relaxation times at 0.19 T of the FR (black circles) and SR (red circles). The solid lines account for the best fits considering the simultaneous presence of direct + Orbach mechanisms for the FR process (blue) and Orbach + Raman for the SR process (green).

The second process was fitted to a sum of Orbach and Raman processes, leading to the following parameters: B = 284(50) s^{-1}K$^{-1.4}$, n = 1.4(1); τ_0 = 2.6(5)·10^{-7} s and U_{eff} = 48(1) K.

Complex **3** presents two sets of Dy^{III} ions concerning to the Dy-donor distances. The first set comprising Dy1, Dy2 and Dy3 ions. Each of these ions contains only one Dy-$O_{phenoxido}$ bond with the shortest Dy-O distance, which are in the 2.248Å-2.263Å range, respectively. The rest of distances in each coordination sphere are greater than 2.4 Å. The second set of Dy ions, Dy4, Dy5 and Dy6, do not contain any coordinated phenoxido group, so that the shortest Dy-O distances involve the enolate and μ_3-nitrate oxygen atoms, which are found in the 2.345Å-2.394Å range. As for the first set of Dy ions, the rest of Dy-donor distances are all greater than 2.4 Å. As in the case of **1** and **2** complexes, the shortest Dy-$O_{phenoxido}$ distances cause large crystal effects and a stronger anisotropy. Thus, in the first case a largely axial ground state relatively well separated from the excited states is expected, whereas in the second case a less axial ground state with not so well energy separation from the excited state could be assumed. The existence of these two sets of Dy ions could be the reason why two set of peaks are observed for compound **3** at different temperatures. If so, the first set should correspond to the relaxation process appearing at higher temperatures in the χ''_M vs T plot, whereas the second set with shortest Dy-O distances larger than 2.35 Å should correspond to the relaxation process observed at lower temperatures.

Results from Theoretical Studies:

To understand the magnetic relaxation dynamics and the different relaxation processes offered by the dinuclear(**1**), tetranuclear(**2**), and hexanuclear (**3**) Dy complexes, ab initio CASSCF/RASSI-SO/SINGLE_ANISO/POLY_ANISO calculations have been performed on the crystal structures of the complexes obtained from the X-ray diffraction using the MOLCAS package. All the calculations have been performed in two steps; first, the single-ion anisotropy

has been derived for the individual Dy^{III} centres, and then we proceed to the polynuclear complex using the input from the single-ion calculations.

Mechanism of Magnetization Relaxation Originating from Single-ions: The energy of low lying eight Kramers Doublet (KDs) originating from the $^8H_{15/2}$ for individual Dy^{III} for all three complexes have been provided in table **3** below, along with the ground and first excited state g anisotropy values. It is worth noting that, for complex **1**, both the Dy^{III} ions are asymmetric and offer different ligand fields. Although both the Dy-1 and Dy-2 centres have $\{DyO_6N_3\}$ moiety, the geometrical parameters are very different (see Figure **3**, **7** and **11**; Table **S1**-**S2** of ESI). The ligand field is more axial for Dy-1 centre compared to the Dy-2 centre, and hence the ground to first excited state energy splitting is larger for the former than the latter (144.6 cm^{-1} vs 116.4 cm^{-1}). This is reflected in the crystal field parameters B_2^0 which is larger for Dy-1 than Dy-2 (-2.45

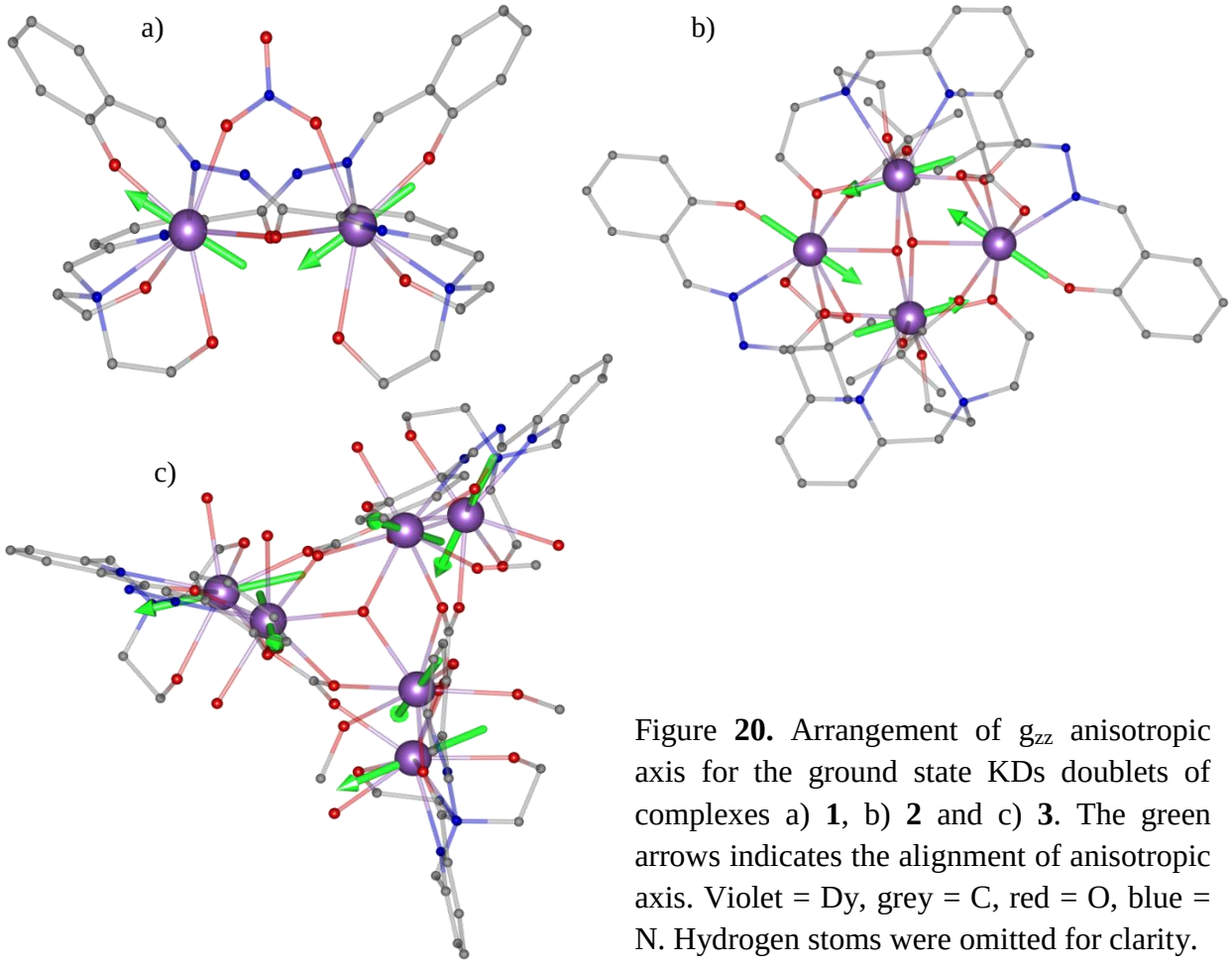

Figure **20.** Arrangement of g_{zz} anisotropic axis for the ground state KDs doublets of complexes a) **1**, b) **2** and c) **3**. The green arrows indicates the alignment of anisotropic axis. Violet = Dy, grey = C, red = O, blue = N. Hydrogen stoms were omitted for clarity.

for Dy-1 and -2.21 for Dy-2, Table **S7**).

Table **3**. Ab initio computed energy of low lying eight KDs along with ground and 1st excited state g-factor for complexes **1**-**3**.

KD	Complex 1		Complex 2		Complex 3					
	Dy-1	Dy-2	Dy-1/3	Dy-2/4	Dy-1	Dy-2	Dy-3	Dy-4	Dy-5	Dy-6
1	0.0	0.0	0.0	0.0	0.0	0.0	0.0	0.0	0.0	0.0
2	144.6	116.4	98.0	157.3	102.0	112.9	110.2	27.2	23.3	30.3
3	217.9	166.2	143.0	259.1	142.4	185.0	156.4	67.4	62.4	76.2
4	298.1	260.9	183.1	301.2	227.8	243.0	229.1	113.6	98.2	101.1
5	372.4	333.9	262.9	374.7	316.3	315.5	309.5	129.5	133.9	134.0
6	422.7	377.3	328.2	441.4	397.0	387.3	377.3	149.4	143.8	158.6
7	464.6	438.7	404.1	557.4	444.3	443.0	427.0	202.8	178.6	194.4
8	602.6	606.9	438.4	775.0	599.8	582.6	529.2	337.7	309.1	343.8
g_{xx}	0.030	0.059	0.083	0.004	0.080	0.052	0.067	0.337	10.923	1.803
g_{yy}	0.060	0.127	0.178	0.007	0.161	0.088	0.115	1.021	8.283	4.078
g_{zz}	19.658	19.437	19.616	19.863	19.347	19.425	19.446	17.750	2.352	15.110
g_{xx}	0.665	1.082	0.956	0.089	11.317	0.823	1.760	2.410	0.593	2.393
g_{yy}	1.434	3.089	1.825	0.127	7.589	1.403	4.399	4.410	3.476	5.324
g_{zz}	15.708	14.107	16.147	17.810	2.138	16.057	14.111	14.195	8.283	8.599

For Dy-1, the ground state anisotropy is purely Ising is nature (g_{zz} =19.658, g_{xx} = 0.03, g_{yy} = 0.06) whereas for Dy-2 a small transverse anisotropy is present in the ground state (g_{zz} =19.437, g_{xx} = 0.06, g_{yy} = 0.13). The ground state is estimated to be m_J=±15/2 for both of the centres, and a strong mixing is observed in the first excited state. This is reflected in their g anisotropy (see table **3**). For both centres, the single ion relaxation is taking place in the first excited via Raman/Orbach or TA-QTM process (see Figure **21**). The ground state anisotropy axis arrangement for each of the Dy^{III} centres has been plotted in Figure **20,** which agrees with the direction predicted from the electrostatic model and based on the shortest Dy-O bond lengths.[16]

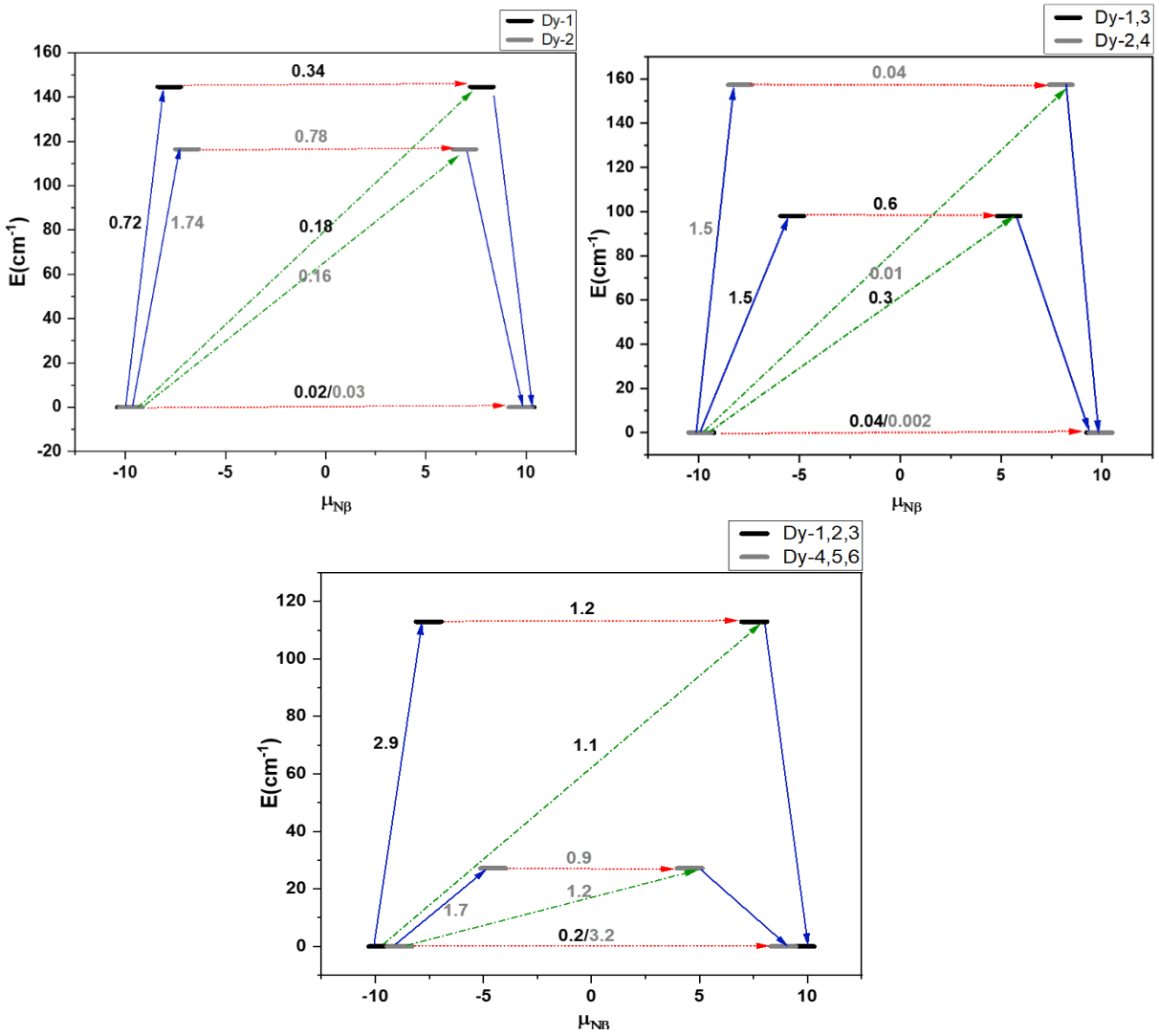

Figure **21**. Magnetic relaxation dynamics through ab initio computation for each of the Dy centers for complexes **1**, **2** and **3** (clockwise). The thick black line represents the Kramers doublets as a function of computed magnetic moment. The green dotted arrows show the possible pathway through Orbach/Raman relaxation; the dotted red lines and blue represent the presence of QTM/TA-QTM between the connecting pairs. The numbers provided at each arrow are the mean absolute value for the corresponding matrix element of the transition

For complex **2**, the two Dy^{III} centres at the wing part (Dy-1 and Dy-3) and two Dy^{III} centres are at the body part(Dy-2 and Dy-4) of the inverse butterfly core are symmetric with respect to each other and exhibit the same single-ion anisotropy. The wing Dy-1 and Dy-3 centres have

{DyO_7N} coordination mode while the body Dy-2 and Dy-4 centres have {DyO_6N_2} coordination from the ligands. Hence the LoProp charge and the crystal field parameters around the corresponding Dy^{III} centres differ dramatically (Table S6 and Figure S20 in ESI), resulting in an ground-first excited state KD energy gaps of 98.0 cm^{-1} (B_2^0 = -1.58) and 157.3 cm^{-1} (B_2^0 = -2.42) for Dy-1/3 and Dy-2/4, respectively. For the Dy-2/4 centers (highly axial, g_{zz} =19.863, g_{xx} = 0.004, g_{yy} = 0.007), the relaxation occurs via the 2nd excited state whereas for the Dy-1/3 (comparatively less axial g_{zz} =19.616, g_{xx} = 0.08, g_{yy} = 0.18) centers, it occurs via the 1st excited state (see figure **21**, Table 3). The individual g anisotropy axis for each of the Dy^{III} centres for complex **2** were plotted in figure **20**. The direction of the ground state g_{zz} axes indicate a circular arrangement and suggests the possibility of observing toroidal moments. The probable S-shape behaviour observed in the M vs H plot further suggests that this complex may exhibit toroidal moments.

Similarly, for complex **3**, the three Dy^{III} centres in the upper triangle structurally resemble each other, and the three Dy^{III} of the lower triangle structurally resemble each other. For the upper triangle, all the three Dy^{III}(Dy-1/2/3) have {DyO_7N} coordination mode, and for the lower triangle Dy^{III}(Dy-4/5/6), {DyO_7N_2} coordination mode was observed. This difference in the coordination number and geometry strongly influence the anisotropy of the metal ions. The Dy^{III} centres at the upper (Dy1-3) triangles show a ground-state-first-excited state KDs energy gap in the range of 102-113 cm^{-1}. The ground state is found to be axial (g_{zz} =19.447-19.347, g_{xx} = 0.05-0-08, g_{yy} = 0.08-0.18, see Table **3**). For the lower triangle, all the Dy^{III} ions exhibit a very large transverse anisotropy at the ground state with the ground-state-first-excited state KDs energy gap is estimated to be in the range of 23 -30 cm^{-1} (Table **3**). For all the six individual Dy^{III} centres, the relaxation is taking place via the 1st excited state (Figure **21**). For both the triangles in

complex **3**, a circular arrangement of the anisotropic axes is absent, and therefore no toroidal moments are expected for this complex.

Despite the presence of strong anisotropy in the ground state and significantly less QTM in the ground state, the observed U_{eff} values for all three complexes are comparatively less than the single ion obtained values for complex **1** (Dy_2, U_{eff} = 60.2 cm^{-1}, $U_{calDy\text{-}1}$ = 144.6 cm^{-1}, $U_{calDy\text{-}2}$ = 116.4 cm^{-1}) and **2** (Dy_4, U_{eff} = 21.5 cm^{-1}, $U_{calDy\text{-}1/3}$ = 98 cm^{-1}, $U_{calDy\text{-}2/4}$ = 157.3 cm^{-1}). For complex **3** the computed values found to lie on both ends compared to experiments (Dy6, U_{eff} = 43 cm^{-1}, $U_{calDy\text{-}1/2/3}$ = 23.3 to 30.3 cm^{-1}, $U_{calDy\text{-}4/5/6}$ = 102 to 112.9 cm^{-1}). To understand the role of exchange coupling in magnetization relaxation, we turn to POLY_ANISO method.

Mechanism of Magnetization Relaxation Originating from the Exchange Coupled States and Observance of SMT behaviour in 2:

The Dy-Dy centres coupling through the oxo bridges often results in weak but non-negligible exchange interactions. For complex **1**, there is a single exchange interaction between the Dy-Dy centres mediating via two μ-O enolate and via a NO_3^- bidentate bridging group and for complex **2**, four different exchange interactions were possible between the Dy1-Dy2, which is equal to Dy3-Dy4 interactions (J_1 mediates via two μ-O atom belonging to a μ_3-OH and μ-enolate groups and a carboxylate bridging group of the pivalate ligand see Figure 22). Similarly, the exchange coupling between the Dy1-Dy4 and Dy2-Dy3 is estimated to be identical, and this is termed as J_2 mediating via a μ_3-OH and an enolate bridging groups (see Figure 22). The J_3 and J_4 interactions between Dy1-Dy3 and Dy2-Dy4 mediate via two μ_3 oxo and long ligand spacer atoms, respectively. We have considered two different exchange interactions for complex **3**: J_1 via the μ_3-OH group and μ_3-OCO_2 group for the Dy1-3 in the upper triangle and J_2 via μ-$O_{enolate}$ and μ_3-OCO_2 between the Dy centres of two triangles (Dy1-Dy4 etc. Figure 22).

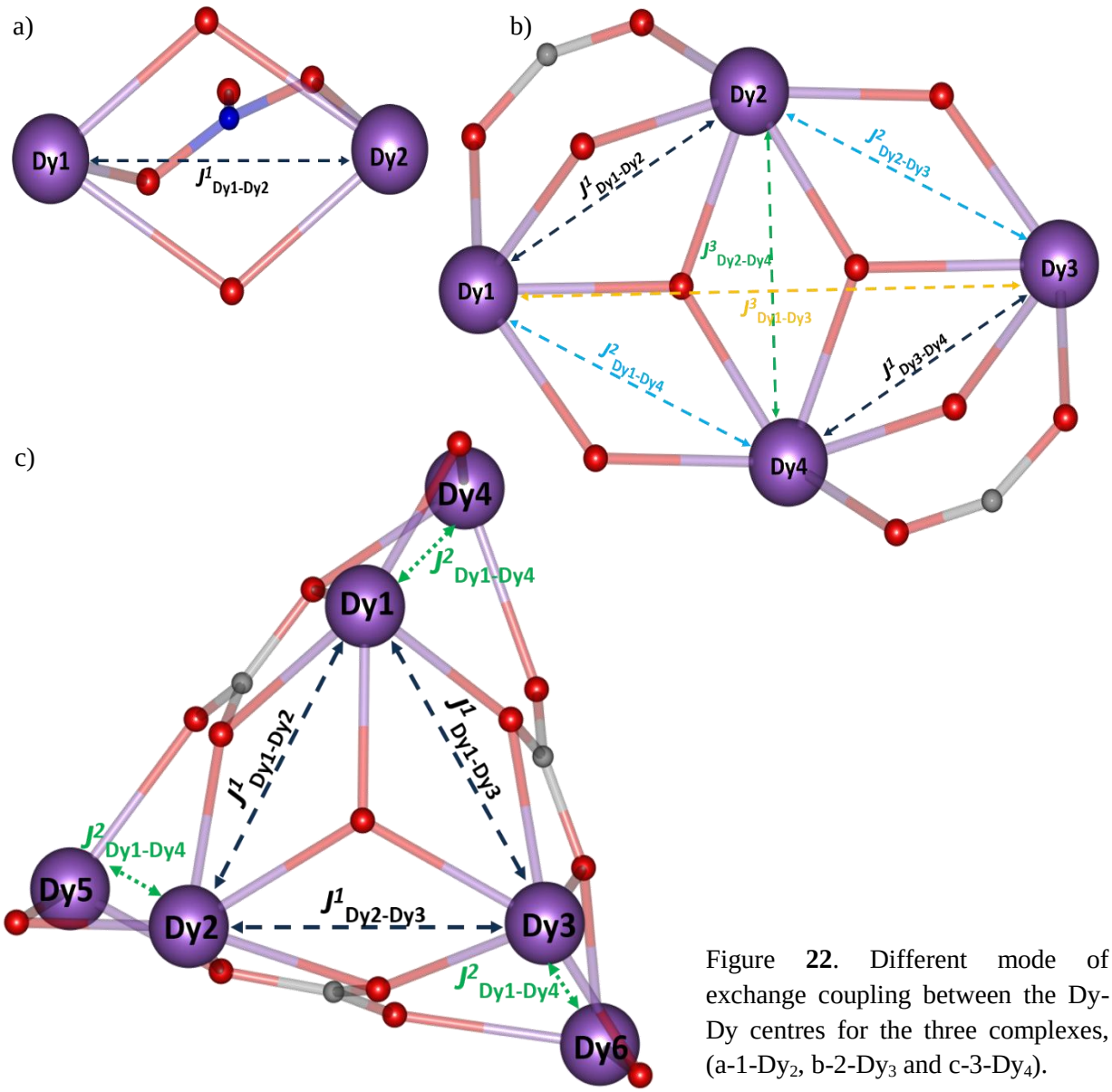

Figure **22**. Different mode of exchange coupling between the Dy-Dy centres for the three complexes, (a-1-Dy_2, b-2-Dy_3 and c-3-Dy_4).

First, the exchange coupling has been estimated using the DFT calculations by replacing the anisotropic Dy^{III} ion with the isotopic Gd^{III} and rescaling it by a factor of 5/7 (see computational details) using the following Hamiltonian represented in equation 6-8 below. This exchange has been used as a starting guess for the POLY_ANISO fitting to derive the magnetic relaxation dynamics for the overall complexes. A simultaneous fit for both susceptibility and magnetization data was performed (solid lines in Figure 15). The Dy…Dy dipolar coupling

estimated using equation 9 has been employed for our calculations. The exchange coupling obtained from the density functional calculations and ab initio POLY_ANISO fitted values are provided in Table **4** below, which are in good agreement with each other. All the exchange coupling calculated are in a similar range for Dy-Dy coupling.

For **1**-Dy_2, $\widehat{H}_{exch} = -J_{Dy1-Dy2}\hat{S}_{Dy1}\hat{S}_{Dy2}$ ..... Equation (6)

For **2**-Dy_4,

$$\widehat{H}_{exch} = -J_{Dy1-Dy3}\hat{S}_{Dy1}\hat{S}_{Dy3} - J_{Dy2-Dy4}\hat{S}_{Dy2}\hat{S}_{Dy4} - 2J_{Dy1-Dy2}\hat{S}_{Dy1}\hat{S}_{Dy2} - 2J_{Dy1-Dy4}\hat{S}_{Dy1}\hat{S}_{Dy4}$$

....Equation (7)

For **3**-Dy_6,

$$\widehat{H}_{exch} = -J_{Dy1-Dy3}\hat{S}_{Dy1}\hat{S}_{Dy3} - J_{Dy2-Dy3}\hat{S}_{Dy2}\hat{S}_{Dy3} - J_{Dy1-Dy3}\hat{S}_{Dy1}\hat{S}_{Dy3} - J_{Dy1-Dy4}\hat{S}_{Dy1}\hat{S}_{Dy4} - J_{Dy2-Dy5}\hat{S}_{Dy2}\hat{S}_{Dy5} - J_{Dy3-Dy6}\hat{S}_{Dy3}\hat{S}_{Dy6}$$ .....Equation (8)

The total exchange is the combination of both the J_{exch} and J_{dipo} using the following equation,

$$\widehat{H} = -(-J_{dip}^{Ln^i - Ln^{i+1}} + J_{exch}^{Ln^i - Ln^{i+1}})\tilde{s}_{Ln_i}\tilde{s}_{Ln_{i+1}}$$ .....Equation (9)

$$J_{dip}^{Ln^i - Ln^{i+1}} = \frac{\mu_B^2}{R^3_{Dy^i - Dy^{i+1}}}\, g_{Ln}^2$$ .....Equation (10)

Table **4**. DFT computed, and POLY_ANISO fitted exchange coupling parameters for complexes **1**, **2** and **3**.

Complex	**1-Dy2**	**2-Dy4**	**3-Dy6**
	-0.021,(J_{dip}=+0.03,	-0.05(J_{dip}=+0.055,	-0.01(J_{dip}=+0.04,

$J^1_{Dy1\text{-}Dy2}$	J_{tot}=+0.009) [-0.02]	J_{tot}=+0.005) [-0.04]	J_{tot}=-0.03)
$J^2_{Dy1\text{-}Dy4}$	---	-0.006(J_{dip}=+0.02, J_{tot}=-0.014)[-0.01]	-0.02(J_{dip}=+0.05, J_{tot}=-0.04)
$J^2_{Dy2\text{-}Dy3}$	---	-0.01(J_{dip}=+0.02, J_{tot}=-0.014)[-0.01]	-0.01(J_{dip}=+0.04, J_{tot}=-0.03)
$J^1_{Dy3\text{-}Dy4}$	---	-0.04 (J_{dip}=+0.045, J_{tot}=+0.005) [-0.05]	-- --
$J^3_{Dy2\text{-}Dy4}$	---	-0.01(J_{dip}=+0.02, J_{tot}=-0.014) [-0.01]	-- --
$J^3_{Dy1\text{-}Dy3}$	---	---	-0.01(J_{dip}=+0.04, J_{tot}=-0.03)
$J^2_{Dy2\text{-}Dy5}$	---	---	-0.02(J_{dip}=+0.05, J_{tot}=-0.04)
$J^2_{Dy3\text{-}Dy6}$	---	---	-0.02(J_{dip}=+0.05, J_{tot}=-0.04)
* The value in the square parenthesis is obtained from the density functional calculations.			

The exchange coupling between Dy-Dy in complex **1** is found to be weakly antiferromagnetic in nature (spin densities are given in Figure S21 for **1** and **2**), whereas the dipolar coupling between the two centres exhibits relatively larger ferromagnetic coupling. The dipolar coupling computed with the POLY_ANISO module is found to be similar to the J_{dip} estimated using the equation 1 (+0.019 vs +0.03). The POLY_ANISO simulation yield U_{cal} = 167 K, though, at the ground state, there are states which have magnetic moments closer to zero magnetic moments (see Figure S22 in ESI) which is likely to offer a very strong QTM process. Although small (4 x 10^{-7} cm^{-1}), the tunnel splitting computed is relatively high enough to offer tunnelling at the ground state, as observed from experiments. This also rationalizes the relatively larger U_{cal} obtained from the calculations compared to the experiment as this estimate obtained from the ab initio

relaxation mechanism did not factor in the tunnelling process at the ground pseudo doublet states.

The probable S shape behaviour of the M vs H curve, along with the arrangement of the single-ion calculated anisotropy axis, indicates the presence of the toroidal magnetic state in complex **2**. The toroidal behaviour for complex **2** has been investigated using the POLY_ANISO module. The flipping of spin and hence the direction of anisotropic axis in the low lying toroidal states have been represented in figure **23**. The observed experimental U_{eff} value is much smaller than the POLY_ANISO computed value for complex **2**. This suggests that weak Dy…Dy coupling is likely to be overcome at the measured temperature leading to the observation of single-ion relaxation. A significant dipolar coupling (+0.02 to +0.045, see Table 4) between the Dy-Dy centres in complex **2** plays a dominating role in determining the toroidal magnetic state as four Dy^{III} centres form a circular arrangement of anisotropy. The local magnetization vector and major anisotropy axis are collinear due to the magnetic exchange, resulting in a non-compensated ground state magnetic moment. As a result, the presence of a toroidal magnetic moment in complex **2** is categorized as a

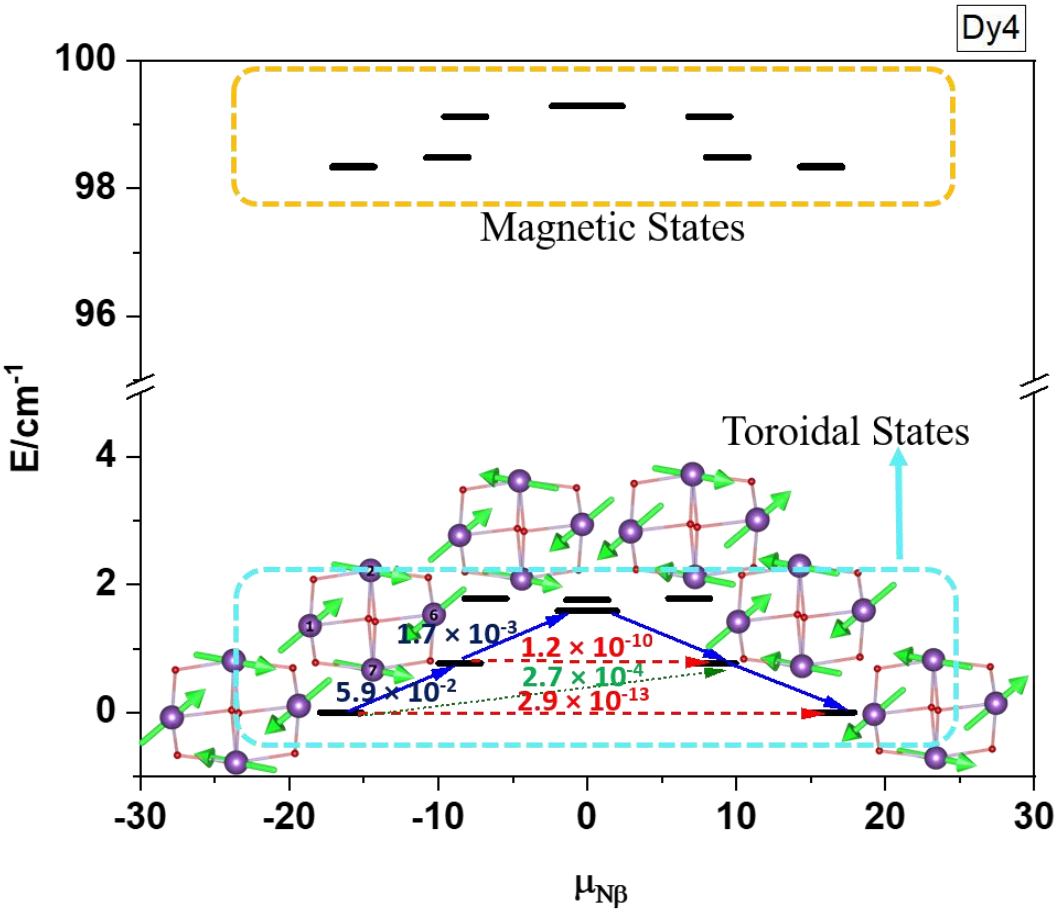

Figure **23**. Poly_aniso generated toroidal states for complex **2**-Dy4.

mixed moment single-molecule toroic due to the dipolar ferromagnetic orientation of the pseudospins on Dy sites and the large magnetic moment of Dy sites in the ground exchange doublet (SMT). However, contrary to this, the arrangement of the anisotropy axis in complex **3** does not indicate any toroidal magnetic state. This is in accord with the experimental field dependence of the magnetization curve, where no S-shape was detected . For complex **3**, no toroidal arrangement was noticed and the POLY_ANISO fitting gives an energy barrier of 29 cm^{-1} which is slightly less compared to the U_{eff} (43 cm^{-1},figure S23).

Conclusion

In summary, we have synthesized three dysprosium complexes with varying nuclearity {Dy_2}, {Dy_4} and {Dy_6} using a flexible arylohydrazone Schiff base ligand by changing the metal to ligand ratio and either the Dy^{III} salt or the base (triethylamine to tetrabutylammonium) in combination with the presence of a coligand. Complex **1** is a dinuclear complex with nine coordinated metal centres and spherical tricapped trigonal prism coordination geometry, while **2** is a tetranuclear complex in a butterfly-shaped topology. **3** is a homometallic hexanuclear assembly where three atmospheric carbon dioxide molecules are trapped in the complex in the form of a carbonate ligand. DC measurements of **1-3** revel that room temperature χ_M T values match good with expected values. AC susceptibility measurements of **1-3** reveal that all the complexes show relaxation of magnetization ~~even~~ in zero applied field. Temperature and field dependence of the relaxation times suggest that that the magnetization relaxation in complex **1** takes place through a combination of QTM, Raman and Orbach processes, while in complex **2** it occurs through QTM and Orbach processes. In the case of complex **3** the relaxation does not take place through QTM but through a combination of Raman and Orbach processes. Complex **1** has U_{eff} and τ_0 values of 87(1) K and $\tau_0 = 6.4(3) \times 10^{-9}$ s, repectively. For complex **2** U_{eff} = 31(2) K, $\tau_0 = 4.2(1) \times 10^{-7}$ s while **3** shows a double relaxation of magnetization [U_{eff1} = 62(3) K, $\tau_{01} = 4.6(3) \cdot 10^{-8}$ s, and U_{eff1} = 2(1) K, $\tau_{02} = 4(6) \cdot 10^{-5}$ s] at zero applied field. Ab Initio calculation suggests that due to the weak magnetic coupling between the metal centres, the magnetic relaxation ~~barrier~~ is dominated by the single Dy^{III} centres rather than the exchange-coupled state. Taking into account this, the dynamic properties of **1-3** can be rationalized on the basis of the shortest Dy-O bonds, their distribution on the Dy^{III} coordination sphere, as well as the different

types of Dy^{III} ions present in the structure. Furthermore, for complex 2, the toroidal magnetic state has been investigated and confirmed with the help of theoretical tools.

References

1. N. Ishikawa, M. Sugita, T. Ishikawa, S.-y. Koshihara and Y. Kaizu, *J. Am. Chem. Soc.*, 2003, **125**, 8694-8695.
2. (a) R. Sessoli and A. K. Powell, *Coord. Chem. Rev.*, 2009, **253**, 2328–2341; (b) D. N. Woodruff, R. E. P. Winpenny and R. A. Layfield, *Chem. Rev.*, 2013, **113**, 5110-5148; (c) A. Dey, P. Kalita and V. Chandrasekhar, *ACS Omega*, 2018, **3**, 9462-9475; (d) Z. H. Zhu, M. Guo, X. L. Li and J. K. Tang, *Coord. Chem. Rev*., 2019, **378**, 350–364; (e) C. A. P. Goodwin, *Dalton Trans.*, 2020, **49**, 14320-14337.
3. (a) H. L. C. Feltham and S. Brooker, *Coord. Chem. Rev.*, 2014, **276**, 1-33; (b) J.-L. Liu, Y.-C. Chen and M.-L. Tong, *Chem. Soc. Rev.*, 2018, **47**, 2431-2453; (c) J. Acharya, P. Kalita and V. Chandrasekhar, *Magnetochemistry*, 2021, **7**, 1; (d) A. Zabala-Lekuona, J. M. Seco and E. Colacio, *Coord. Chem. Rev.* 2021, **441**, 213984 ; (e) V. S. Parmar, D. P. Mills and R. E. P. Winpenny, *Chem. Eur. J.*, 2021, **27**, 7625-7645.
4. (a) C. A. P. Goodwin, F. Ortu, D. Reta, N. F. Chilton and D. P. Mills, *Nature*, 2017, **548**, 439-442; (b) F.-S. Guo, B. M. Day, Y.-C. Chen, M.-L. Tong, A. Mansikkamäki and R. A. Layfield, *Science*, 2018, **362**, 1400.

5. (a) Y.-C. Chen, J.-L. Liu, L. Ungur, J. Liu, Q.-W. Li, L.-F. Wang, Z.-P. Ni, L. F. Chibotaru, X.-M. Chen and M.-L. Tong, *J. Am. Chem. Soc.*, 2016, **138**, 2829-2837; (b) J. Liu, Y.-C. Chen, J.-L. Liu, V. Vieru, L. Ungur, J.-H. Jia, L. F. Chibotaru, Y. Lan, W. Wernsdorfer, S. Gao, X.-M. Chen and M.-L. Tong, *J. Am. Chem. Soc.*, 2016, **138**, 5441-5450; (c) S. K. Gupta, T. Rajeshkumar, G. Rajaraman and R. Murugavel, *Chem. Sci.*, 2016, **7**, 5181-5191; (d) Y.-S. Ding, N. F. Chilton, R. E. P. Winpenny and Y.-Z. Zheng, *Angew. Chem. Int. Ed.*, 2016, **55**, 16071-16074; (e) Z. Jiang, L. Sun, Q. Yang, B. Yin, H. Ke, J. Han, Q. Wei, G. Xie and S. Chen, *J. Mater. Chem. C*, 2018, **6**, 4273-4280.
6. (a) S. Biswas, K. S. Bejoymohandas, S. Das, P. Kalita, M. L. P. Reddy, I. Oyarzabal, E. Colacio and V. Chandrasekhar, *Inorg. Chem.*, 2017, **56**, 7985-7997; (b) A. K. Bar, P. Kalita, J.-P. Sutter and V. Chandrasekhar, *Inorg. Chem.*, 2018, **57**, 2398-2401; (c) P. Kalita, A. Malakar, J. Goura, S. Nayak, J. M. Herrera, E. Colacio and V. Chandrasekhar, *Dalton Trans.*, 2019, **48**, 4857-4866; (d) P. Kalita, N. Ahmed, A. K. Bar, S. Dey, A. Jana, G. Rajaraman, J.-P. Sutter and V. Chandrasekhar, *Inorg. Chem.*, 2020, **59**, 6603-6612; (e) P. Kalita, P. Nayak, N. Ahmed, J. M. Herrera, K. Venkatasubbaiah, E. Colacio and V. Chandrasekhar, *Dalton Trans.*, 2020, **49**, 15404-15416. (f) I. F. Díaz-Ortega, J. M. Herrera, S. Dey, H. Nojiri, G. Rajaraman, Enrique Colacio, *Inorg. Chem. Front.*, 2020,**7**, 689-699
7. (a) Y.-N. Guo, G.-F. Xu, W. Wernsdorfer, L. Ungur, Y. Guo, J. Tang, H.-J. Zhang, L. F. Chibotaru and A. K. Powell, *J. Am. Chem. Soc.*, 2011, **133**, 11948-11951; (b) J. Long, F. Habib, P.-H. Lin, I. Korobkov, G. Enright, L. Ungur, W. Wernsdorfer, L. F. Chibotaru and M. Murugesu, *J. Am. Chem. Soc.*, 2011, **133**, 5319-5328; (c) J. D. Rinehart, M. Fang, W. J. Evans and J. R. Long, *J. Am. Chem. Soc.*, 2011, **133**, 14236-14239; (d) E. Moreno

Pineda, N. F. Chilton, R. Marx, M. Dörfel, D. O. Sells, P. Neugebauer, S.-D. Jiang, D. Collison, J. van Slageren, E. J. L. McInnes and R. E. P. Winpenny, *Nature Commun.*, 2014, **5**, 5243; (e) J. D. Rinehart, M. Fang, W. J. Evans and J. R. Long, *Nature Chem.*, 2011, **3**, 538-542; (f) F.-S. Guo and R. A. Layfield, *Chem. Commun.*, 2017, **53**, 3130-3133; (g) L. Zhang, Y.-Q. Zhang, P. Zhang, L. Zhao, M. Guo and J. Tang, *Inorg. Chem.*, 2017, **56**, 7882-7889; (h) T. Han, Y.-S. Ding, Z.-H. Li, K.-X. Yu, Y.-Q. Zhai, N. F. Chilton and Y.-Z. Zheng, *Chem. Commun.*, 2019, **55**, 7930-7933.; (i) J. Acharya, N. Ahmed, J. Flores Gonzalez, P. Kumar, O. Cador, S. K. Singh, F. Pointillart and V. Chandrasekhar, *Dalton Trans.*, 2020, **49**, 13110-13122. P. Kumar, S. Biswas, A. Swain, J. Acharya, V. Kumar, P. Kalita, J. F. Gonzalez, O. Cador, F. Pointillart, G. Rajaraman and V. Chandrasekhar, *Inorg. Chem.*, 2021, **60**, 8530-8545.

8. (a) M. Evangelisti and E. K. Brechin, *Dalton Trans.*, 2010, **39**, 4672-4676; (b) G. Lorusso, M. A. Palacios, G. S. Nichol, E. K. Brechin, O. Roubeau and M. Evangelisti, *Chem. Commun.*, 2012, **48**, 7592-7594; (c) R. Sessoli, *Angew. Chem. Int. Ed.*, 2012, **51**, 43-45; (d) J.-L. Liu, Y.-C. Chen, F.-S. Guo and M.-L. Tong, *Coord. Chem. Rev.*, 2014, **281**, 26-49; (e) X.-M. Luo, Z.-B. Hu, Q.-f. Lin, W. Cheng, J.-P. Cao, C.-H. Cui, H. Mei, Y. Song and Y. Xu, *J. Am. Chem. Soc.*, 2018, **140**, 11219-11222; (f) S.-J. Liu, S.-D. Han, J.-P. Zhao, J. Xu and X.-H. Bu, *Coord. Chem. Rev.*, 2019, **394**, 39-52.
9. (a) S. Das, S. Hossain, A. Dey, S. Biswas, J.-P. Sutter and V. Chandrasekhar, *Inorg. Chem.*, 2014, **53**, 5020-5028; (b) S. Biswas, S. Das, T. Gupta, S. K. Singh, M. Pissas, G. Rajaraman and V. Chandrasekhar, *Chem.Eur. J.*, 2016, **22**, 18532-18550; (c) S. Biswas, S. Das, J. Acharya, V. Kumar, J. van Leusen, P. Kögerler, J. M. Herrera, E. Colacio and V. Chandrasekhar, *Chem. Eur. J.*, 2017, **23**, 5154-5170; (d) S. Biswas, P. Kumar, A.

Swain, T. Gupta, P. Kalita, S. Kundu, G. Rajaraman and V. Chandrasekhar, *Dalton Trans.*, 2019, **48**, 6421-6434; (e) P. Kumar, S. Biswas, A. Swain, J. Acharya, V. Kumar, P. Kalita, J. F. Gonzalez, O. Cador, F. Pointillart, G. Rajaraman and V. Chandrasekhar, *Inorg. Chem.*, 2021, **60**, 8530-8545.

10. (a) A. I. Vogel, B. S. Furniss, A. J. Hannaford, P. W. G. Smith and A. R. Tatchell, *Vogel's textbook of practical organic chemistry. 5th ed*, Longman, Harlow, 1989; (b) D. B. G. Williams and M. Lawton, *J.Org. Chem.*, 2010, **75**, 8351-8354.
11. (a) SMART and SAINT, Software Reference manuals, Version 6.45, 2003; (b) G. M. Sheldrick, University of Göttingen: Göttingen, Germany, 2.05 edn., 2002; (c) SHELXTL Reference Manual; Bruker Analytical X-ray Systems, Inc., Madison, WI, 2000; (d) CrysAlis PRO, Rigaku Oxford Diffraction, Yarnton, England, 2015; (e) G. Sheldrick, A short history of SHELX, *Acta Crystallogr. Sect. A*, 2008, **64**, 112-122; (f) O. V. Dolomanov, L. J. Bourhis, R. J. Gildea, J. A. K. Howard and H. Puschmann, OLEX2: *J.App.Crystallogr.*, 2009, **42**, 339-341; (g) K. Bradenburg, Diamond, version 3.1 e, *Crystal Impact GbR: Bonn, Germany*, 2005.
12. (a) K. Sołtys-Brzostek, M. Terlecki, K. Sokołowski and J. Lewiński, *Coord. Chem. Rev.*, 2017, **334**, 199-231; (b) P. Mateus, R. Delgado, F. Lloret, J. Cano, P. Brandão and V. Félix, *Chem. Eur. J.*, 2011, **17**, 11193-11203; (c) J. C. Anderson, A. J. Blake, R. B. Moreno, G. Raynel and J. van Slageren, *Dalton Trans.*, 2009, 9153-9156; (d) A. K. Ghosh, M. Pait, M. Shatruk, V. Bertolasi and D. Ray, *Dalton Trans.*, 2014, **43**, 1970-1973; (e) S. Titos-Padilla, J. Ruiz, J. M. Herrera, E. K. Brechin, W. Wersndorfer, F. Lloret and E. Colacio, *Inorg. Chem.*, 2013, **52**, 9620-9626; (f) J. Goura, E. Colacio, J. M. Herrera, E. A. Suturina, I. Kuprov, Y. Lan, W. Wernsdorfer and V. Chandrasekhar,

Chem. Eur. J., 2017, **23**, 16621-16636. (g) T. D. Pasatoiu, A. Ghirri, A. M. Madalan, M. Affronte and M. Andruh, *Dalton Trans.*, 2014, **43**, 9136-9142; (h) S. K. Langley, B. Moubaraki and K. S. Murray, *Inorg. Chem.*, 2012, **51**, 3947-3949; (i) P. C. Andrews, T. Beck, C. M. Forsyth, B. H. Fraser, P. C. Junk, M. Massi and P. W. Roesky, *Dalton Trans.*, 2007, 5651-5654; (j) R. J. Holmberg, C.-J. Kuo, B. Gabidullin, C.-W. Wang, R. Clérac, M. Murugesu and P.-H. Lin, *Dalton Trans.*, 2016, **45**, 16769-16773; (k) M. Hołyńska, R. Clérac and M. Rouzières, *Chem. Eur. J.*, 2015, **21**, 13321-13329; (l) H. Tian, L. Zhao and J. Tang, *Crys, Growth Des.*, 2018, **18**, 1173-1181; (m) W.-M. Wang, Z.-L. Wu, Y.-X. Zhang, H.-Y. Wei, H.-L. Gao and J.-Z. Cui, *Inorg. Chem. Front.*, 2018, **5**, 2346-2354.

13. (a) J. Cirera, E. Ruiz and S. Alvarez, *Organometallics*, 2005, **24**, 1556-1562; (b) *SHAPE: Continuous Shape Measures calculation 2.1; Electronic Structure Group*, Universitat de Barcelona: Spain, 2013.
14. (a) P. Kalita, J. Goura, J. Manuel Herrera Martínez, E. Colacio and V. Chandrasekhar, *Eur. J. Inorg. Chem.*, 2019, **2019**, 212-220; (b) Y. Bi , Y.-N. Guo, L. Zhao, Y. Guo, S.-Y. Lin, S.-D. Jiang, J. Tang, B.-W. Wang and S. Gao, *Chem. Eur. J.*, 2011, **17**, 12476-12481; (c) H. L. C. Feltham, Y. Lan, F. Klöwer , L. Ungur, L. F. Chibotaru, A. K. Powell and S. Brooker, *Chem. Eur. J.*, 2011, **17**, 4362-4365.
15. M. M. Hänninen, A. J. Mota, D. Aravena, E. Ruiz, R. Sillanpää, A. Camón, M. Evangelisti and E. Colacio, *Chem. Eur. J*, 2014, **20**, 8410-8420.
16. N. F. Chilton, D. Collison, E. J. L. McInnes, R. E. P. Winpenny and A. Soncini, *Nat. Commun.*, 2013, **4**, 2551-2557.

17. (a) Y.-N. Guo, X.-H. Chen, S. Xue and J. Tang, *Inorg. Chem.*, 2011, **50**, 9705-9713; (b) L. Zou, L. Zhao, P. Chen, Y.-N. Guo, Y. Guo, Y.-H. Li and J. Tang, *Dalton Trans.*, 2012, **41**, 2966-2971; (c) D. Maniaki, P. S. Perlepe, E. Pilichos, S. Christodoulou, M. Rouzières, P. Dechambenoit, R. Clérac and S. P. Perlepes, *Molecules*, 2020, **25**, 3153.
18. M. Sutradhar, E. C. B. A. Alegria, T. R. Barman, M. F. C. Guedes da Silva, C.-M. Liu and A. J. L. Pombeiro, *Frontiers in Chemistry*, 2020, **8**, 157.
19. K. N. Shrivastava, *phy. status solidi (b)*, 1983, **117**, 437-458.
20. N.M. Chilton, CCFIT Program; The Chilton Group: Manchester, UK, 2014.